RSC Advances

PAPER

View Article Online
View Journal | View Issue

Cite this: *RSC Adv.*, 2024, **14**, 38615

Enhanced magnetoresistance properties of K-site deficient $La_{0.85}K_{0.1}\square_{0.05}MnO_3$ manganites synthesized *via* sol–gel, wet-mixing, and solid-state reaction methods

Okvarahireka Vitayaya,[a] Budhy Kurniawan, *[a] Phahul Zhemas Zul Nehan,[a] Dicky Rezky Munazat,[a] Toto Sudiro,[b] Agung Imaduddin,[b] Heri Nugraha,[d] Sigit Dwi Yudanto [e] and Maykel T. E. Manawan[bc]

The effect of synthesis methods on the structural, magnetic, electrical transport, and magnetoresistance (MR) properties of K-deficient $La_{0.85}K_{0.1}\square_{0.05}MnO_3$ (LK_dMO) materials has been investigated. The compounds were synthesized *via* sol–gel (SG), wet-mixing (WM), and solid-state (SS) reaction. The resulting ceramics were characterized using X-ray diffraction (XRD), scanning electron microscopy (SEM), energy dispersive spectroscopy (EDS), X-ray photoelectron spectroscopy (XPS), and four point probe (FPP) techniques to evaluate their crystal structure, morphologies, elemental composition, electrical transport properties, and magnetoresistance (MR) behavior. This study reveals that the electrical- and magneto-transport properties of LK_dMO ceramics are strongly influenced by their synthesis method. Among the samples, the WM method yielded ceramics with smaller grain sizes and more dispersed grain boundaries, leading to reduced resistivity. The MR values for LK_dMO ceramics synthesized through SG, WM, and SS reached 17.05% at 287.74 K, 54.68% at 271.50 K, and 47.09% at 270.25 K, respectively. The WM-synthesized sample exhibited superior crystal quality and enhanced magnetic and electrical properties. These results indicate that LK_dMO ceramics are promising candidates for application in magnetic sensors.

Received 3rd October 2024
Accepted 18th November 2024

DOI: 10.1039/d4ra07105k

rsc.li/rsc-advances

1. Introduction

Lanthanum manganite materials $La_{1-x}AE_xMnO_3$ (where AE represents alkaline earth ions) have been extensively studied because of their wide range of applications, including data storage, magnetic sensors, magnetic refrigeration, and spintronics.[1–4] Doping with divalent or monovalent ions at the La site or doping Mn with 3d transition ions can lead to change from antiferromagnetic type-A to various states, such as ferromagnetic metals (FMMs), ferromagnetic insulators (FMIs), and antiferromagnetic insulators (AFMIs).[5] Doped lanthanum manganites exhibit intriguing phenomena, such as magnetoresistance (MR) and the magnetocaloric effect (MCE), which depend on the ionic radii of the A-site ion[6–10] and Mn^{3+}/Mn^{4+}.[11] Substitution of divalent or monovalent ions at the La^{3+} site introduces mixed valence states of Mn (Mn^{3+} and Mn^{4+}).[12] Replacing divalent alkaline earth metals (such as Ba^{2+}, Sr^{2+}, and Ca^{2+}) with monovalent ions (such as Na^+, Ag^+, and K^+) results in significant changes in the mixed valence of manganese, leading to enhanced double exchange (DE) interactions and induction of colossal magnetoresistance (CMR).[13,14] Doping with monovalent ions (K^+) at the La^{3+} site, for each amount of K, twice the amount of Mn^{3+} ions is oxidized to Mn^{4+}, resulting in an excess of Mn^{3+} regions around La^{3+} and excess Mn^{4+} regions around K^+ ions. This indicates that even a small amount of dopant can generate a large number of charge carriers, thereby enhancing conductivity.[15–17] Deficiencies at the A-site in the perovskite structure lead to an increased number of Mn^{4+} ions and changes in the ionic radii of the A-site $\langle r_A \rangle$, which affect the Mn–O bond length and the Mn–O–Mn bond angle, thus increasing DE interaction and T_C.[18] Cation vacancies at the A-site also affect the physical properties of manganites, such as their magnetic and transport properties.[19,20]

Research on the colossal magnetoresistance (CMR) effect, particularly in perovskite manganite materials with mixed valence states, has garnered significant attention in recent years.[21–23] The ferromagnetic properties of the material enhance the movement of conduction electrons and reduce the kinetic

[a]*Department of Physics, Universitas Indonesia, Depok, 16424, Indonesia. E-mail: budhy.kurniawan@sci.ui.ac.id*

[b]*Research Center for Advanced Material, National Research and Innovation Agency (BRIN), South Tangerang City, 15314, Indonesia*

[c]*Faculty of Defense Technology, Indonesia Defense University, Bogor 16810, Indonesia*

[d]*Research Center for Energy Conversion and Conservation, National Research and Innovation Agency, Indonesia*

[e]*Center for Metallurgy, National Research and Innovation Agency, Indonesia*

energy. CMR is associated with electron transport and is influenced by variations in magnetic structures induced by an external magnetic field.[24] The CMR effect is influenced by the internal stress resulting from variations in the ionic radii of constituent ions,[25] grain boundaries,[26,27] grain size,[28] crystallinity,[29] and tunnel junctions resulting from doping.[30] Oxides based on $LaMnO_3$ exhibited high MR values under low field influence. Different synthesis preparation methods result in different properties of manganites.[31–34] Experimental conditions can significantly influence various parameters that affect the physical properties of manganite materials.[35–37] The most commonly used synthesis method for manganite materials is the solid-state reaction (SS) method. This method requires higher annealing temperatures and longer holding times to achieve a homogeneous composition and desired structure.[38,39] Recently, chemical reaction methods requiring lower preparation temperatures and improved sample homogeneity have been developed,[32] such as the sol–gel method.[35–37] Additionally, the wet-mixing (WM) method is more efficient than the sol–gel (SG) method because it does not require additional precursors, such as citric acid for metal ion complexation, and results in less mass loss during heating. WM is a straightforward and promising method for low-cost material production.[34] The properties of manganites continue to attract attention and development because of their excellent physical properties and potential applications in devices.[40] Therefore, it is crucial to understand how synthesis methods affect various aspects of the physical properties of manganite.[32] Lik *et al.* reported differences in properties such as T_C and MR, which are highly influenced by the grain size and crystallinity affected by the synthesis method of the sample.[41] In 2021, Jin *et al.* reported a maximum MR value of 46.39% at room temperature (293.03 K) for $La_{1-x}K_xMnO_3$ with $x = 0.15$, attributed to the double exchange (DE) mechanism and tunneling effects.[42] Additionally, the formation of vacancies in $LaMnO_3$-based materials can lead to increased MR values. Dhahri *et al.* reported that $La_{1-x}\square_xMnO_3$ with $x = 0.2$ achieved an MR value of nearly 85% at 255 K.[43] In 2021, Yu *et al.* investigated the influence of synthesis methods on the electrical transport properties of $La_{0.67}Ca_{0.33}MnO_3$ material using the solid-state reaction and sol–gel methods. The MR value of LCMO ceramics was found to be 39.97% at a temperature of 246.78 K and 54.27% at a temperature of 263.80 K for the solid-state and sol–gel samples, respectively, with the application of a 1 T magnetic field.[44] In Lik *et al.*'s research, they also compared the effect of synthesis methods on $La_{0.7}Sr_{0.3}MnO_3$ ceramics synthesized using SG and SS methods, yielding maximum MR values of 22% and 18% at a temperature of 80 K, respectively.[41] In 2013, Pan *et al.* successfully prepared $La_{0.85}K_{0.15}MnO_3$ ceramics using variations of the solid-state (SS), sol–gel (SG), and co-precipitation (CP) methods and then compared the electron transport properties of the material. The MR values obtained were 6%, 3.5%, and 8%, respectively, at a temperature of 300 K under a 1 T applied magnetic field.[45]

Research on lanthanum manganites has attracted considerable interest due to their promising applications in fields such as magnetoresistance and energy technology. Although significant developments and progress have been made, challenges remain in optimizing magnetic and transport properties. Various solutions continue to be explored, such as doping effects and synthesis techniques. Based on the literature mentioned above, potassium-doped lanthanum manganites (LKMO) and doping in the form of vacancies have shown promising potential due to the possibility of enhanced magnetoresistance. Moreover, systematic studies comparing the effects of different synthesis methods on the transport properties of lanthanum manganites remain limited. Therefore, this study aims to address these gaps by investigating $La_{0.85}K_{0.1}\square_{0.05}MnO_3$ (LK_dMO) synthesized using several methods, such as sol–gel, wet-mixing, and solid-state reaction, to identify the most optimal synthetic method. By focusing on these aspects, this study fundamentally aims to answer unresolved questions about optimizing the magnetoresistance of lanthanum manganite-based materials and to tackle existing challenges in this field of materials science. Therefore, this study explores the effects of different synthesis routes on manganese oxide, focusing on the high magnetoresistance (MR) of ceramic K-deficient $La_{0.85}K_{0.1}\square_{0.05}MnO_3$ (LK_dMO). The crystal structure, morphology, electrical transport properties, and magnetic properties of LK_dMO materials obtained using the SG, WM, and SS methods were compared and discussed.

2. Experimental

2.1 Sol–gel (SG) method

LK_dMO samples were synthesized by SG using high purity La_2O_3, KNO_3, and $Mn(NO_3)_2\cdot 4H_2O$. All the raw materials were stirred and dissolved in deionized water, nitric acid, ethylene glycol, and citric acid. Citric acid was used as a catalyst in the synthesis process, whereas ethylene glycol acted as a chelating agent. Each dissolved base material was then mixed and stirred using a magnetic stirrer at a speed of 500 rpm, and the solution temperature was adjusted to the range of 75–80 °C for the nitric acid evaporation process. After the materials were mixed, the pH of the solution was adjusted by gradually adding an ammonia solution until the pH reached 7. Next, the process was continued with a heat treatment. The dehydration process was carried out at a temperature of 190 °C for 2 h to dry the sample and eliminate the water content within it. Subsequently, the process proceeded to calcination, wherein the sample was placed in a crucible and heated to 600 °C for 6 h in a furnace to remove any remaining organic substances. Next, the sample was ground and subjected to a pre-sintering process at 900 °C for 12 h. The powdered samples were compacted under a pressure of 10 t to form pellets. Finally, sintering was performed again with the sample in pellet form at 1200 °C for 24 h.

2.2 Wet-mixing (WM) method

LK_dMO samples were synthesized *via* WM using high purity La_2O_3, KCO_3, and $MnCO_3$. All raw materials were mixed and dissolved using nitric acid (HNO_3) in a beaker, which was stirred using a magnetic stirrer at a speed of 500 rpm within a temperature range of 75–80 °C until the solution formed

a precipitate. The precipitate was then dehydrated in an oven at 190 °C for 2 h to remove the solvent. The dry sample was ground using a mortar and pestle to form a powder. The powder was then subjected to calcination at 600 °C for 6 h. After calcination, the sample was ground again and pre-sintered at 900 °C for 12 h. Following pre-sintering, the powder was compacted under a pressure of 10 t to form pellets. Finally, sintering was performed on the pellet-form sample at 1200 °C for 24 h.

2.3 Solid-state reaction (SS) method

LK_dMO samples were synthesized *via* SS using high purity La_2O_3, KCO_3, and $MnCO_3$. All raw materials were ground using a mortar for 30 min. The resulting powder was then calcined at 600 °C for 6 h. After calcination, the powder was ground again and subjected to pre-sintering at 900 °C for 12 h. Following pre-sintering, the powder was compacted under 10 tons of load to form pellets. Finally, sintering was performed on the pellet samples at 1200 °C for 24 h. The synthesis process flow of the SG, WM, and SS methods is illustrated in Fig. 1.

2.4 Characterization

The crystal structures and phases were identified using X-ray diffraction (Bruker AXS, D8) with Cu Kα ($\lambda = 1.5406$ Å) radiation in the 2θ range of 20°–90°. The surface morphology of LK_dMO and elemental analysis were examined using scanning electron microscopy (SEM, Hitachi). The magnetic behavior was evaluated using a vibrating sample magnetometer (VSM, SQUID-VSM) with a magnetic field of 1 T at room temperature. The elemental compositions were identified using X-ray photoelectron spectroscopy (XPS) using an Axis Supra + Kratos Analytical system with photon energy radiation Al Kα ($\lambda = 1486.6$ eV). The resistivity was measured and evaluated by applying the four point probe (FPP) method using a Cryogenic Magnet (Oxford Teslatron instrument) in the temperature range of 50–300 K under 0 and 2 T applied magnetic fields.

3. Results and discussion

3.1 Crystal structure

The X-ray diffraction (XRD) patterns of LK_dMO samples synthesized using the sol–gel (SG), wet-mixing (WM), and solid-state (SS) methods and compared with those of the parent compound ($La_{0.85}K_{0.15}MnO_3$ (LKMO)) are shown in Fig. 1(a), and the FWHM shifts of the LK_dMO and LKMO samples are illustrated in Fig. 2(b). As depicted in Fig. 2, it is confirmed that the substitution of vacancies at the K site, amounting to 0.05, did not alter the crystal structure of the parent compound. According to the XRD data, all the samples exhibited a rhombohedral crystal structure with $R\bar{3}c$ space group (no. 167). However, the SG sample also showed the presence of a secondary Mn_2O_3 phase with an orthorhombic crystal structure (*Pbca*). Figure 2 shows that the broadening and full width at half maximum (FWHM) in the LK_dMO samples synthesized by the wet-mixing (WM) and solid-state (SS) methods are smaller, with higher intensity compared to the parental compound

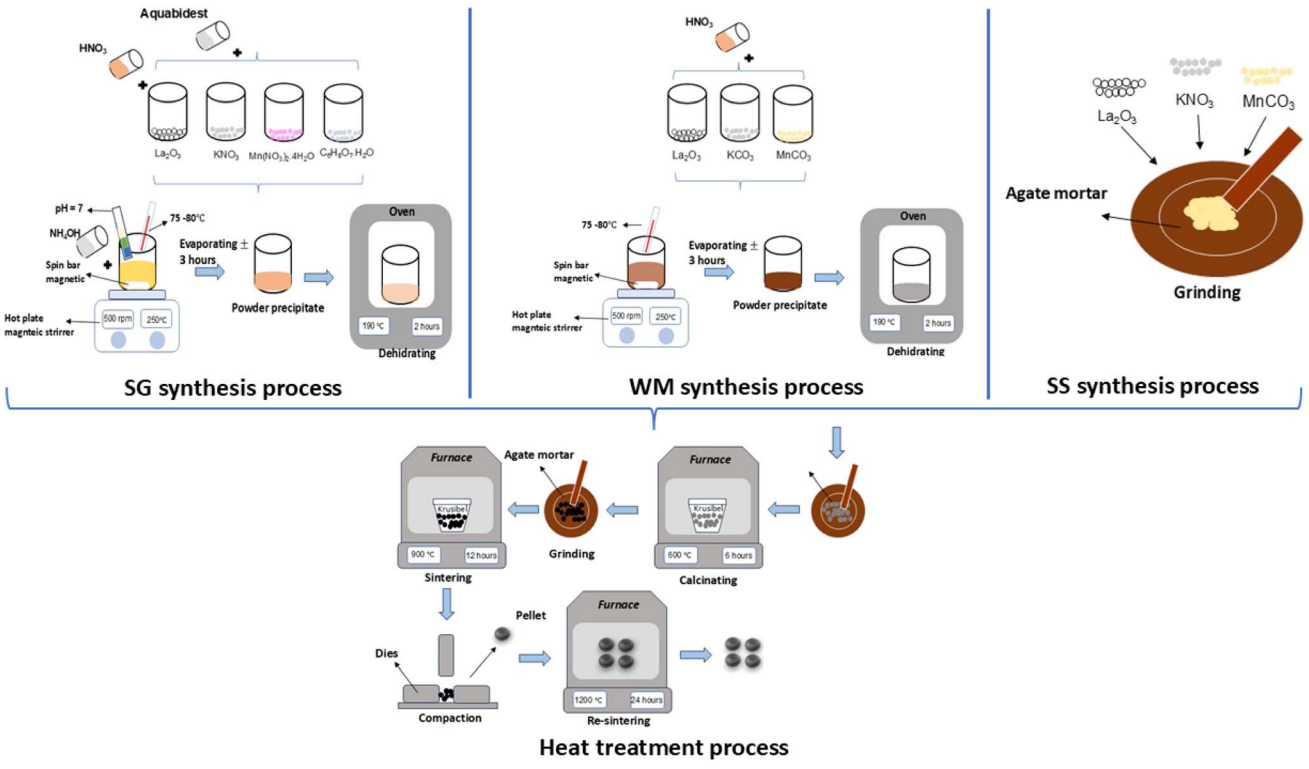

Fig. 1 Process flow of the SG, WM, and SS methods.

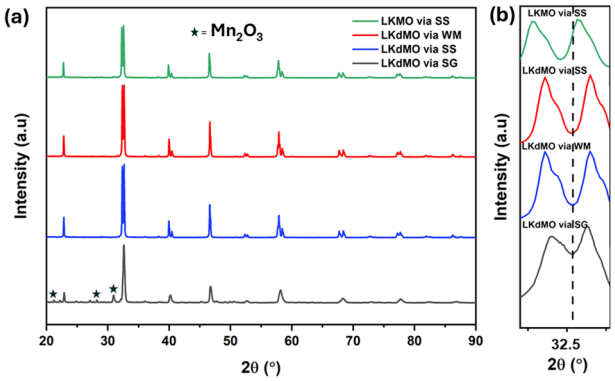

Fig. 2 (a) XRD patterns of the LK_dMO compounds synthesized *via* SG, WM, and SS and parental compound (LKMO) *via* the SS method, (b) FWHM shift of the LK_dMO and parental compound (LKMO) samples.

LKMO. This indicates that the growth of K-deficient formations promotes crystallinity and enhances crystal properties.[46]

The unit cell volumes of each sample were not significantly different. The deficiency of La ions at the A site led to a reduction in the unit cell volume, which was attributed to the increased presence of Mn^{4+} ions in the compound. The ionic radius of Mn^{4+} (0.53 Å) is smaller than that of Mn^{3+} (0.645 Å).[47] However, a deficiency of K^+ ions results in an increase or decrease in the unit cell volume, which cannot be explained solely by the number of Mn^{4+} ions. This phenomenon is associated with the ionic radius of the vacancies at the A site, which may be larger or smaller than that of K^+. Changes in the unit cell volume influence the Mn–O bond length, Mn–O–Mn bond angle, and electron movement between Mn^{3+} and Mn^{4+}, which are significantly affected by the deficiency at the A site in manganite compounds.[48] Substitution with K ions and vacancies results in the replacement of some lanthanum ions by K ions. Because K has a different ionic radius than La, combined with the formation of vacancies, this leads to lattice distortions in the crystal, resulting in deviations in the Mn–O–Mn bond angles and distances. These distortions cause an overlap between Mn and O, which plays an important role in electron mobility and magnetic interactions. Potassium doping and vacancy formation introduce strain due to changes in lattice symmetry, affecting electron hopping.[49–51] In manganite materials, crystal strain affects changes in the electronic bandwidth, making the material more responsive to magnetic fields and potentially increasing the MR value.[52] K ions have a lower valency than La, and vacancy formation also causes the A-site to lack the energy to stabilize, thus affecting the Mn^{3+}/Mn^{4+} ratio. This can increase the number of charge carriers, facilitating electron hopping between Mn^{3+} and Mn^{4+}. This increased electron hopping will improve conductivity, as charge carriers move more easily. The presence of Mn^{3+} and Mn^{4+} ions is necessary to strengthen electron transfer and magnetic coupling.[52]

The XRD characterization data were further analyzed using Rietveld refinement with FullProf software. The Rietveld refinement curves for the experimental data are shown in Fig. 3. The Rietveld refinement results confirmed that the samples had a rhombohedral structure with an $R\bar{3}c$ space group. The Goodness of fit (χ^2) value indicated that the WM sample had a value close to 1, suggesting a better fit and good agreement with the XRD profile than the SG and SS samples. The use of the wet-mixing (WM) method is more efficient than the sol–gel (SG) method. The WM method does not require additional precursors or chelating agents to complex metal ions; thus, less mass is lost during the combustion process.[34] Additionally, the amount of water used during WM synthesis was reduced, leading to a shorter mixing duration. The WM method, using nitric acid as a solvent, allows the use of a wide variety of carbonate precursors, including both soluble and insoluble carbonates. However, the SG method is limited to soluble precursors.[53] It is possible that the wet-mixing method enables WM to produce crystals with better quality than the sol–gel (SG) and solid-state reaction (SS) methods. In the WM method, the use of nitric acid as a solvent and a simpler mixing process allows for a more uniform distribution of precursors, enabling the crystallization process to occur more optimally. Additionally, the minimal mass loss during combustion and shorter synthesis time may contribute to the formation of crystals with better quality compared with the SG and SS methods.

Table 1 presents the lattice parameters for all samples, which did not exhibit significant differences. The differences in the lattice parameters and unit cell volumes among the samples may be attributed to the deficiencies in the constituent elements and variations in the Mn^{3+}/Mn^{4+} ratio, which are influenced by different synthesis methods. The different synthesis methods for L_dKMO material do not create significant differences in the crystal structure. The atomic positions of each element are as follows: La and K occupy position 6a $(0, 0, \frac{1}{4})$, Mn occupies position 6b (0, 0, 0), and O occupies position 18e $(x, 0, \frac{1}{4})$. The presence of a size disorder due to the influence of different methods affects lattice strain, causing oxygen ions to undergo random displacements. This leads to MnO_6 octahedral distortion and electron localization.[54] The c parameter shows a trend of varying values, with values ranging from 13.38850 to 13.96530 Å. This variation is associated with the presence of lattice strain during different synthesis treatments.[55] From the XRD data, the theoretical density of the sample can also be calculated and determined using the equation $\rho_{theo} = \frac{MZ}{NV}$, where M is molecular mass, Z is the number of units per unit cell ($Z = 6$, for rhombohedral structure), N is Avogadro's number ($N = 6.02 \times 10^{23}$), and V is the unit cell volume.[51] Based on the calculations, the density values for each sample do not show significant differences, as the only varying parameter is the unit cell volume, which does not differ greatly among the samples. The theoretical density of the LK_dMO sample is 6.36 g cm^{-3} for all method variations, and 6.39 g cm^{-3} for parental compound (LKMO), a value within the density range of manganite-based materials, as previously reported.[51]

Notably, the unit cell volume of the SG sample was larger than those of the WM and SS samples. This is influenced by variations in the Mn–O bond length (d_{Mn-O}) and Mn–O–Mn angle ($\theta_{Mn-O-Mn}$) related to the Mn^{3+} and Mn^{4+} ratios and the A-site deficiency due to K^+ ion substitution. The stability of the

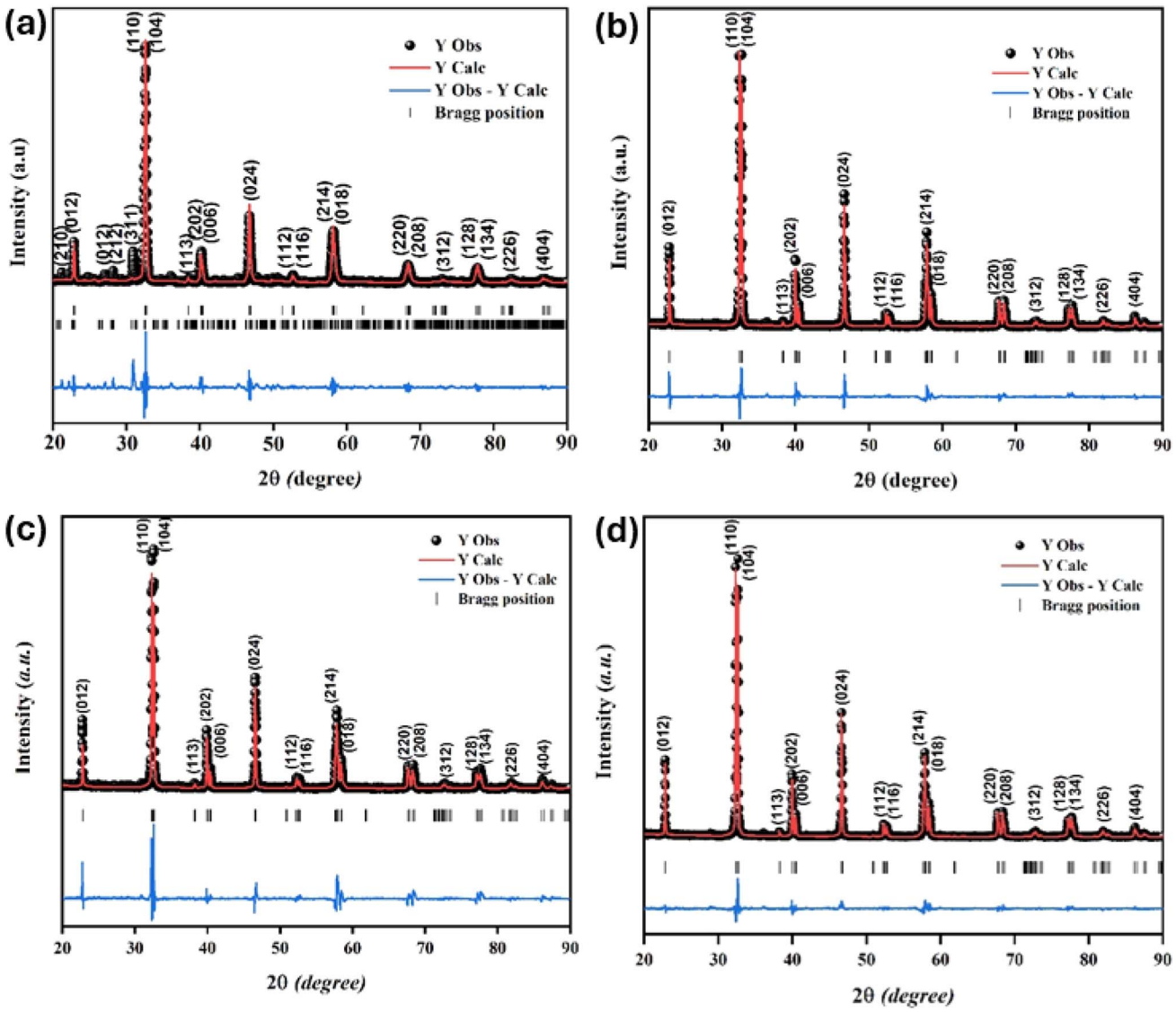

Fig. 3 Rietveld refinement diffraction patterns of the LK_dMO compound synthesized using (a) SG, (b) WM, and (c) SS, and (d) the parental compound (LKMO).

Table 1 Lattice parameters of the $La_{0.85}K_{0.1}\square_{0.05}MnO_3$ sample using the SG, WM, and SS methods

	$La_{0.85}K_{0.1}\square_{0.05}MnO_3$			$La_{0.85}K_{0.15}MnO_3$
Parameter	SG	WM	SS	SS
Space group	$R\bar{3}c$	$R\bar{3}c$	$R\bar{3}c$	$R\bar{3}c$
$a = b$ (Å)	5.50309	5.52841	5.52974	5.53631
c (Å)	13.39260	13.96530	13.36940	13.38850
Volume unit cell (Å^3)	353.9079	353.8879	354.0397	355.3885
$\langle D_S \rangle$ (nm)	121.0237	79.8912	82.1216	65.6190
$\langle D_{W-H} \rangle$ (nm)	180	151	166	138
d_{Mn-O} (Å)	1.9692	1.9653	1.9670	1.9663
$\theta_{Mn-O-Mn}$ (°)	160.7	164.1	163.5	164.8
$R_{profile}$ (%)	36.6	19.9	15.4	34.3
R_{wp} (%)	39.4	22.3	17.8	33.0
Goodness of fit (χ^2)	4.62	1.82	2.34	1.77

perovskite structure with the ABO_3 formula in manganites was predicted using the Goldschmidt tolerance factor equation defined as $t = \frac{\langle r_A \rangle + r_O}{\sqrt{2}(\langle r_B \rangle + r_O)}$, where $\langle r_A \rangle$ is the average ionic radius of the A-site, $\langle r_B \rangle$ is the average ionic radius of the B-site, and $\langle r_O \rangle$ is the ionic radii of oxygen. Ionic size mismatch in the crystal structure leads to a decrease in the symmetry. An ideal cubic structure was achieved when 't' = 1. A tolerance factor in the range of 't' = 1 within the range of $0.90 < t < 1$ indicates that the crystal structure experiences rhombohedral distortion. This reduction was due to the rotation of the adjacent MnO_6 octahedron in opposite directions along the cubic (111) axis. If 't' = 1 within the range $0.75 < t < 0.90$, the distortion increases, leading to an orthorhombic symmetry change caused by octahedron bending inconsistent with the MnO_6 octahedron rotation around the (110) and (104) planes. For the LK_dMO samples, a tolerance factor (t) value of 0.962 was obtained, indicating that

the LK_dMO ceramics had a rhombohedral crystal structure, which is consistent with the XRD analysis. The rhombohedral structure is evidenced by the presence of a doublet intensity in the 2θ range of 32.4 in the XRD pattern due to the (110) and (104) planes. Such peak splitting is characteristic of a rhombohedral crystal structure.[17]

The average crystallite size from the XRD characterization results was calculated by applying the Scherrer method using the following equation:

$$D_S = \frac{K\lambda}{\beta_{hkl}\cos\theta}, \quad (1)$$

where D_S is the average crystallite size, K is the shape factor constant (0.9), λ is the X-ray wavelength of Cu Kα ($\lambda = 1.5406$), and β_{hkl} is the full width at half maximum (FWHM) of the highest intensity peak in the XRD pattern, measured in radians. The crystallite sizes calculated using the Scherrer method are listed in Table 1. The average crystallite sizes (D) calculated using the Debye–Scherrer method (D_S) for the SG, WM, and SS samples were 121.02, 79.89, and 82.12 nm, respectively.

In addition to the Scherrer method, the crystallite size was calculated using the Williamson–Hall method (D_{W-H}). This method assumes that the microstrain is uniform along the crystallographic direction, which makes it isotropic. The β_{hkl} is the FWHM of the Bragg peak in radians and is calculated using the following equation:

$$\beta_{hkl}\cos(\theta) = 4\varepsilon\sin(\theta) + \frac{K\lambda}{D_{W-H}}, \quad (2)$$

where D_{W-H} is the crystallite size and ε is the microstrain of the sample, calculated from the slope and intercept of the plot of $\beta\cos(\theta)$ *vs.* $4\sin(\theta)$. The results of the W–H plot are shown in Fig. 4. The y-axis represents the value considered for each diffraction peak of the sample. A good linear fit across all values resulted in a straight line, where the crystallite size was obtained from the y-intercept, and the microstrain was derived from the slope of the line. It should be noted that β_{hkl} (FWHM in radians) of each peak with intensity was measured using Gaussian function fitting.[56] The average crystallite sizes (D) calculated using the Williamson–Hall method (D_{W-H}) for the SG, WM, and SS samples were 180, 161, and 166 nm, respectively. The SG sample exhibits a larger crystallite size, which was influenced by the FWHM values at higher (2θ) angles, resulting in higher crystallinity compared to the WM and SS samples. Teixeira *et al.* also noted that the SS method has a maximum crystallite size limitation of 100 nm.[57] The crystallite size calculated using the Williamson–Hall method (D_{W-H}) was larger than that obtained using the Scherrer method (D_S) because of the neglect of strain-induced broadening effects in the Scherrer method (D_S).[58]

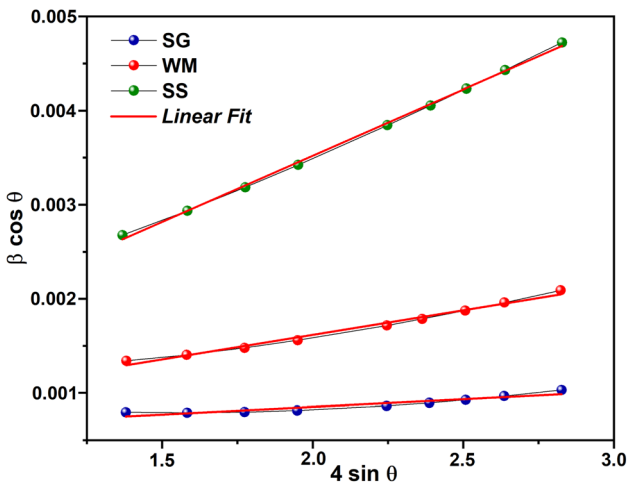

Fig. 4 W–H plot results.

3.2 Surface morphology

SEM images of the LK_dMO sample synthesized by the SG, WM, and SS methods and the parental compound (LKMO) are shown in Fig. 5. The SEM images also indicate that the substitution of K deficiency in LK_dMO does not alter the morphology of the parent compound's structure. All samples consisted of large and small grains ranging from spherical to truncated hexagonal shapes. The differences in the grain size of the LK_dMO samples synthesized using different methods were investigated. The average grain sizes of the LK_dMO by SG, WM, SS, and LKMO are 3.08 μm, 2.25 μm, 3.79 μm, and 3.65 μm, respectively. The grain size produced in each sample is found to be larger than the average crystal size. This indicates that each particle observed in the SEM measurements consists of several crystalline grains.[59,60]

These results are within a reasonable range compared to previous experiments by Wei *et al.* and Shaikh *et al.*, who reported grain sizes of 1–2 μm for $La_{0.8-x}K_{0.2}Mn_{1+x}O_3$ using the SG method[61] and 2–3 μm for $La_{1-x}K_xMnO_3$ ($x = 0.1$, 0.125, and 0.15) using the SS method.[62] The SS sample had a larger average grain size than those of the SG and WM samples. Fig. 5 shows that the SS sample exhibits poor contraction, indicated by non-uniform grain sizes, while the SG sample shows significant differences in grain size, with more uniform grains. Therefore, the sol–gel method is effective in enhancing the uniformity of the grain size in LK_dMO ceramic samples. This is because the SS sample had some grains that coagulated into larger grains.[45] An increase in grain size can enhance electrostatic strength, which leads to a reduction in the lattice parameters $a = b$ and affects the unit cell volume.[63] Furthermore, lattice strain increases proportionally with grain size. The crystal lattice strain can directly impact the lattice parameters $a = b$ as well as the unit cell volume, constricting the lattice.[64]

Furthermore, the WM sample showed smaller grain sizes than the SG sample. This was because the SG method was carried out under neutral pH conditions, while the WM method was carried out under acidic conditions because the precursor was dissolved using nitric acid. Therefore, the pH conditions and the addition of a chelating agent are parameters that affect the grain size differences of each sample.[34] In the process of crystal and grain formation, the pH of the solution during the synthesis has a significant influence. A higher pH supports the growth of larger crystals and grains, which promotes the formation of higher porosity and reduces the density. Meanwhile, smaller and more compact grains are produced at lower or more acidic pH levels, thereby decreasing porosity and increasing density.[65,66] This

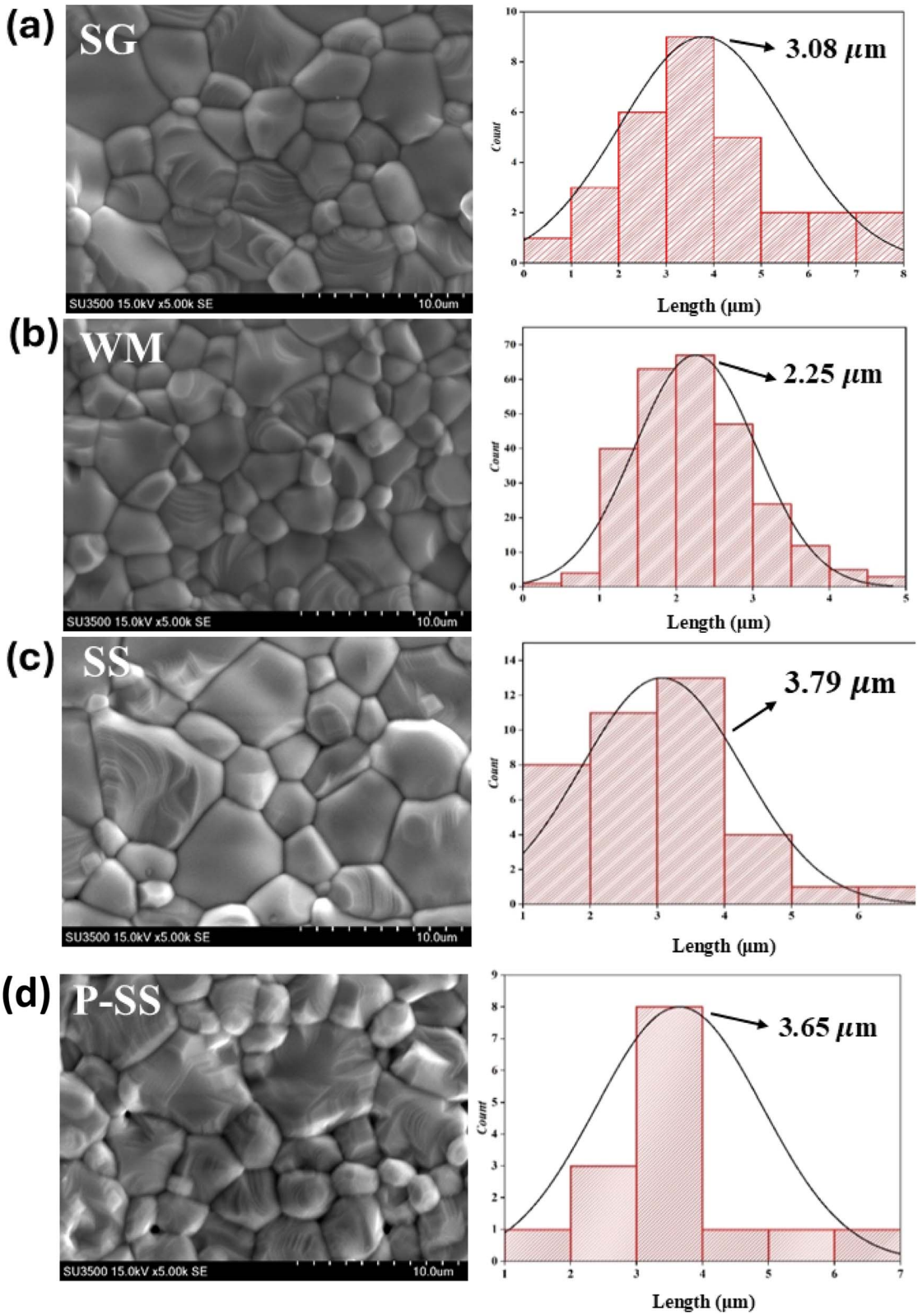

Fig. 5 SEM images of the $La_{0.85}K_{0.1}\square_{0.05}MnO_3$ compound synthesized *via* (a) SG, (b) WM, and (c) SS, and (d) the parental compound *via* SS.

correlation is evident in this study, where the SG sample with a higher solution pH (pH = 7) exhibits larger crystal and grain sizes than the WM sample, which has a solution with a pH of less than 7. The SG sample may also produce greater porosity, reducing the quality of the grains formed. The grain size produced in each sample is found to be larger than the average

crystal size. This indicates that each particle observed in the SEM measurements consists of several crystalline grains.[59,60] An increase in grain size can enhance electrostatic strength, which leads to a reduction in the lattice parameters $a = b$ and affects the unit cell volume.[63] Furthermore, lattice strain increases proportionally with grain size. The crystal lattice strain can directly impact the lattice parameters $a = b$ as well as the unit cell volume, constricting the lattice.[64]

The resistivity of a material is influenced by intra-grain and inter-grain electron transfers. The electron transport properties within the grains can be explained by the double-exchange (DE) mechanism and the Jahn–Teller effect. Following intra-grain electron transport, the grain boundary (GB) became the main factor affecting resistivity. Smaller grain sizes result in more GBs, which leads to increased scattering at GBs and domain boundaries, thus causing an increase in the resistivity of the materials.[44]

To confirm the elemental composition and surface distribution, energy dispersive X-ray spectroscopy (EDS) analysis was conducted, with the data collected, as shown in Fig. 6. Fig. 6 shows the EDS patterns and elemental distribution of the LK_dMO samples synthesized by applying the SG, WM, and SS methods. The SG, WM, and SS samples exhibited a uniform distribution of La, K, Mn, and O in the LK_dMO ceramics. From the EDS results, the atomic percentages of the elements La, K, Mn, and O were obtained. These percentages are compared with the XPS characterization and further stoichiometric calculations.

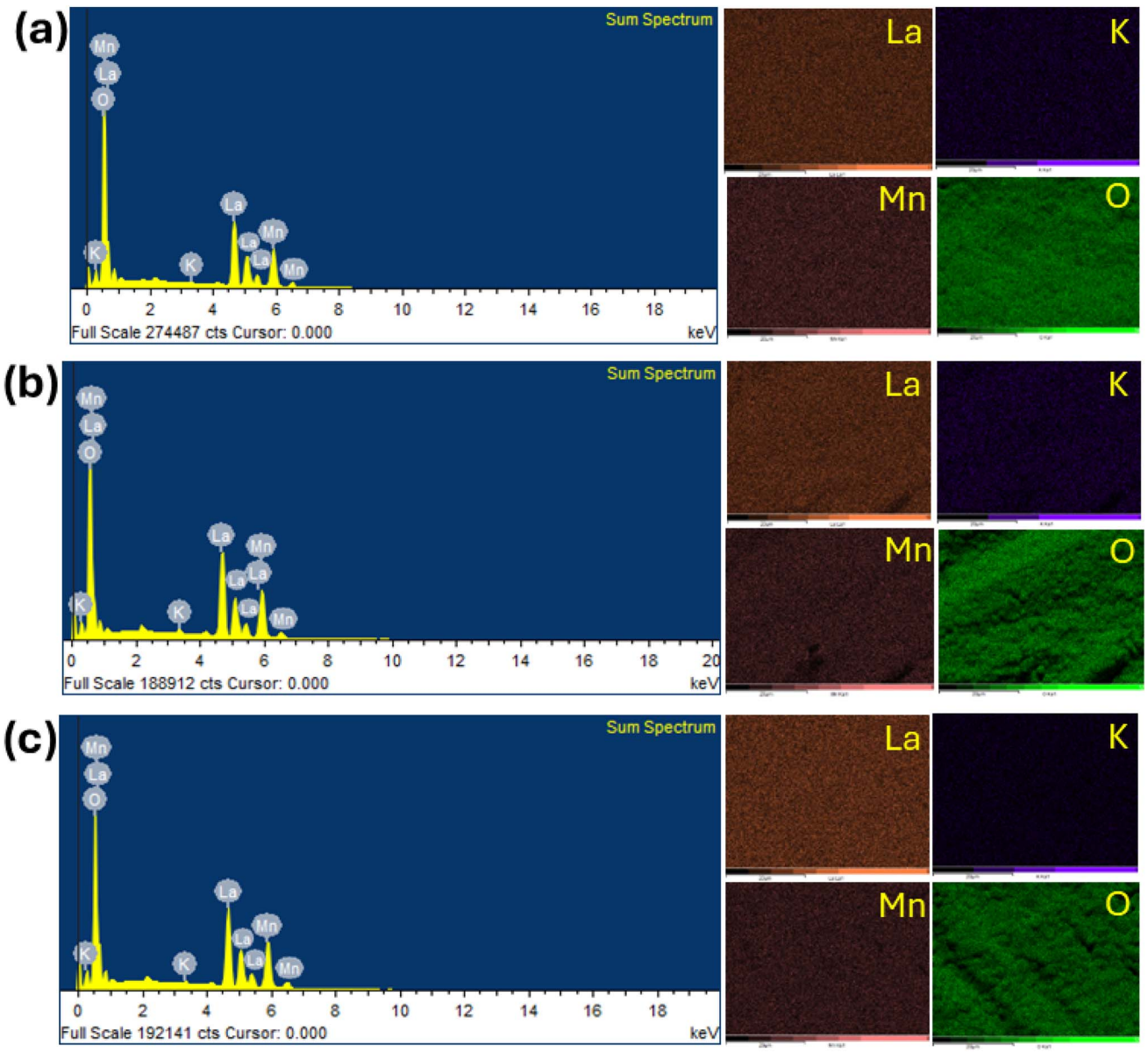

Fig. 6 Elemental mapping image and EDS spectrum of LK_dMO compounds synthesized by (a) SG, (b) WM, and (c) SS methods.

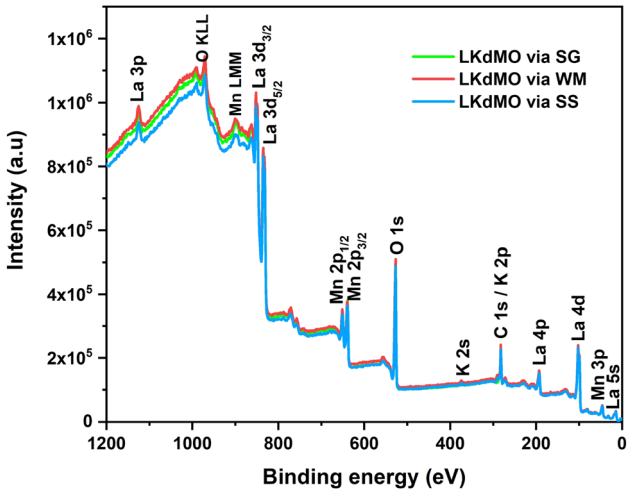

Fig. 7 XPS survey spectrum of LK_dMO compounds.

3.3 X-ray photoelectron spectroscopy (XPS)

The chemical valence states of the LK_dMO ceramics were characterized by XPS, and the results are shown in Fig. 7. Peaks corresponding to La, K, Mn, and O appeared in the XPS spectra. A carbon peak (C 1s) was observed owing to a layer of carbon contamination. This could be because carbon often accumulates as a contaminant on the surface of samples, and XPS has a high surface detection efficiency. The XPS spectra were calibrated using a reference C 1s peak at a binding energy of 284.6 eV. Carbon often accumulates as a contaminant on sample surfaces, even in electron microscopy. Many previous studies also use the C 1s peak of carbon (typically around 284.8 eV) as a reference point for calibrating binding energy in XPS spectra because it is frequently present on surfaces exposed to air, making it a practical and easily accessible standard.[67] This approach simplifies calibration, especially when there is no well-defined internal standard within the sample itself.

The spectra also show Auger peaks at binding energies of 973 and 900 eV, which are associated with Mn (LMM) and O (KLL), respectively. The narrow-scan spectra for La 3d, K 2p, Mn 2p, and O 1s are presented in Fig. 8–11, respectively. The XPS spectra were analyzed using ESCape software, applying Gaussian–Lorentzian profiles, a Shirley background for the La and Mn spectra, and a linear background for the K and O spectra. The atomic ratios obtained from the XPS results are summarized in Table 2 and compared with the EDS results. Table 2 indicates that K-deficiency was successfully formed in the LK_dMO sample for all the synthesis method variations. This is evidenced by the atomic percentages of La, K, Mn, and O, which closely matched the stoichiometric calculations for $La_{0.85}K_{0.1}\square_{0.05}MnO_3$. The synthesis process for LK_dMO used high-purity precursors (≥99.9%) and was conducted in a controlled atmosphere to minimize contaminants across all

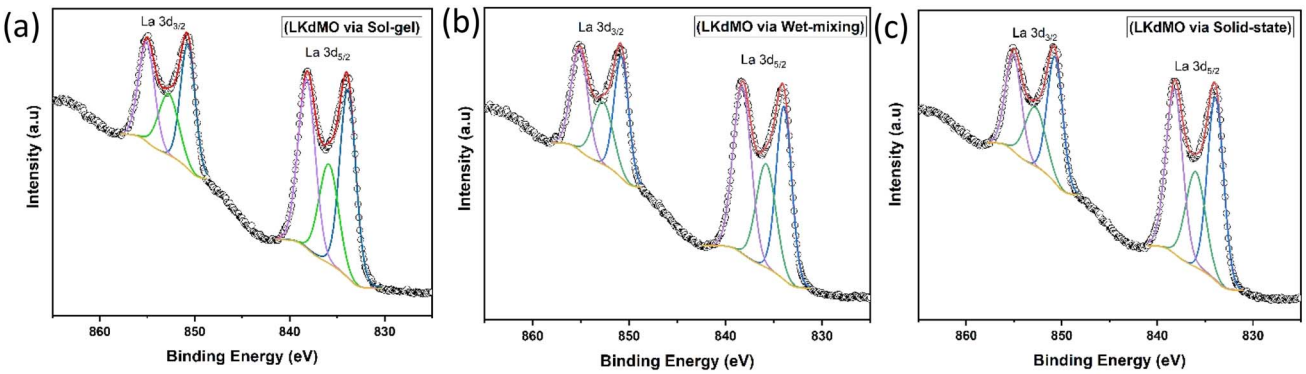

Fig. 8 Narrow scan of La 3d XPS spectra of LK_dMO samples synthesized using (a) SG, (b) WM, and (c) SS methods.

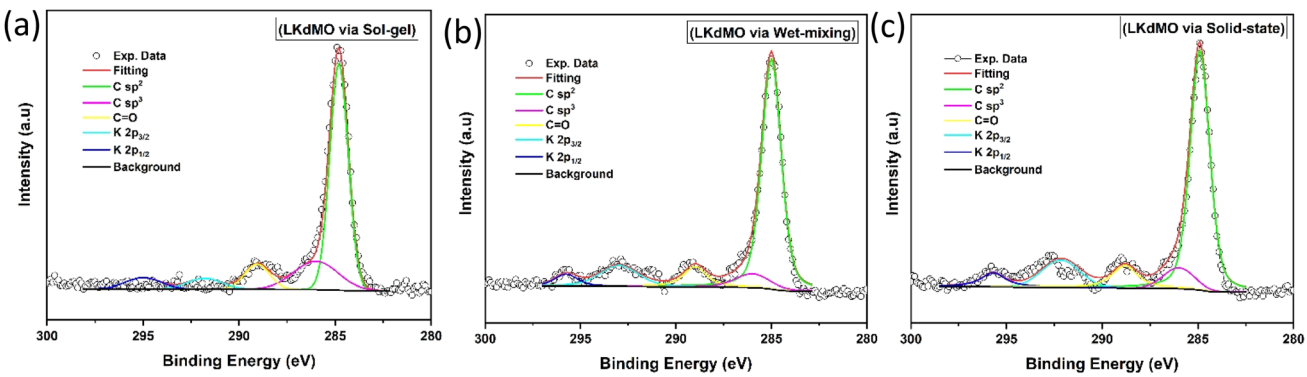

Fig. 9 Narrow scan of K 2p and C 1s XPS spectra of LK_dMO samples synthesized using (a) the SG, (b) WM, and (c) SS methods.

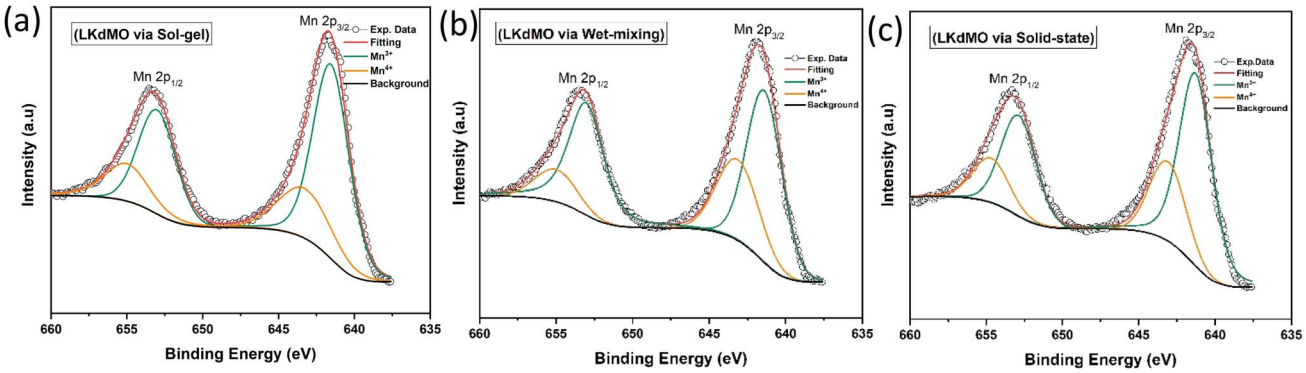

Fig. 10 Narrow scan of Mn 2p XPS spectra of LK_dMO samples synthesized *via* (a) the SG, (b) WM, and (c) SS methods.

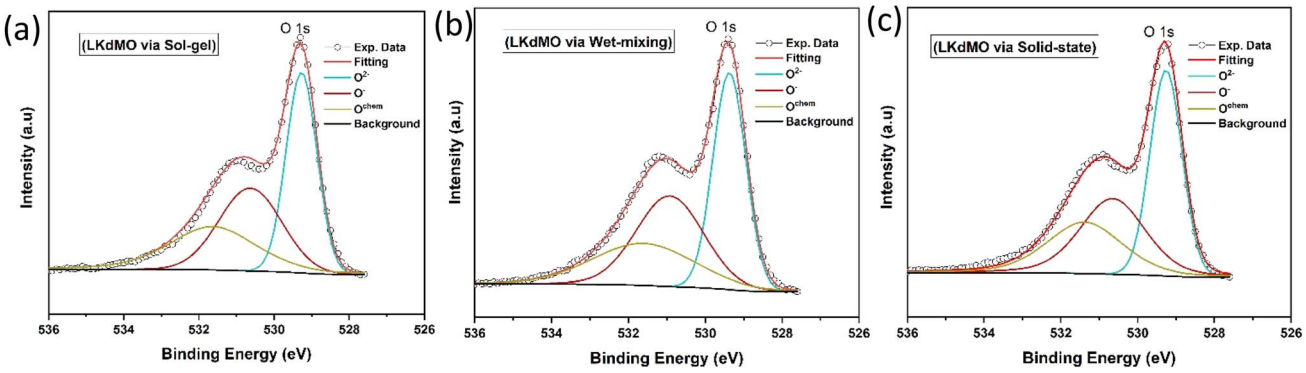

Fig. 11 Narrow scan of O 1s XPS spectra of LK_dMO samples synthesized *via* (a) the SG, (b) WM, and (c) SS methods.

method variations. XRD analysis showed that the samples formed a single phase, except for the SG sample, which had a slight secondary phase (Mn_2O_3). Carbon contamination detected by XPS likely resulted from environmental exposure, but it had a minimal impact on MR and magnetic properties. The composition observed from XPS analysis aligned with theoretical values, confirming the successful formation of K-deficiency, which enhances magnetoresistance through modifications in Mn–O–Mn bonding and charge carrier density.

The properties of ceramics are significantly influenced by the grain boundaries (GB).[68,69] The O^{2-} ions in the Mn–O–Mn bonds at the GB tend to become unstable and prone to separation from the structure, creating oxygen vacancies. These oxygen vacancies were the main reason for the elemental distribution discrepancies observed in the EDS results. Although different synthesis methods were used, the peak positions of each constituent element in the XPS spectra remained constant.

Fig. 8 shows the La 3d core level, which forms a doublet structure, specifically La $3d_{5/2}$ and La $3d_{3/2}$, at binding energies of approximately 833.8 eV and 850.7 eV, respectively. The separation between the La 3d peaks is 16.9 eV, which is similar to the value reported in the literature.[58] After deconvolution of the La 3d spectrum, an energy separation of approximately 4.4 eV for La $3d_{5/2}$ and 4.3 eV for La $3d_{3/2}$, respectively, were observed. Weak peaks induced during charge transfer were identified as satellite peaks. These La 3d spectra are typical of the manganite oxide family.

Table 2 EDS and XPS results of $La_{0.85}K_{0.1}\square_{0.05}MnO_3$ synthesised using the SG, WM dan SS methods

		Atomic %			
Samples	Ratio	La	K	Mn	O
$La_{0.85}K_{0.1}\square_{0.05}MnO_3$ (SG)	EDS	15.89	0.04	15.57	68.59
	XPS	17.3	2.6	19.9	60.20
$La_{0.85}K_{0.1}\square_{0.05}MnO_3$ (WM)	EDS	17.58	0.36	17.16	64.90
	XPS	17.0	2.4	19.9	60.70
$La_{0.85}K_{0.1}\square_{0.05}MnO_3$ (SS)	EDS	18.29	0.66	17.39	63.66
	XPS	17.2	2.2	20.30	60.4
$La_{0.85}K_{0.1}\square_{0.05}MnO_3$	Stoichiometry	17.17	2.03	20.20	60.60
$La_{0.85}K_{0.15}MnO_3$ (parental)	Stoichiometry	17	3	20	60

XPS is a method conducted on the surface that provides information about the outermost 10 nm layer, including the carbon surface content, metal content, metal distribution, and chemical state of elements. The binding energy range around carbon (284–289 eV) allows for the identification of various compounds. Deconvolution of the C 1s spectrum reveals components corresponding to C–C bonds at 284.9 eV, C=O bonds at 286–287 eV, and O=C–O bonds in carbonates at 288–289 eV. Additionally, peaks at 292.2 eV and 295.0 eV represent K $2p_{3/2}$ and K $2p_{1/2}$, respectively (Fig. 9). The K 2p peaks cause

a shift in the C 1s peak to lower binding energies due to the dipole formation caused by the electronegativity differences between K and C, which are 0.8 and 2.5, respectively.[70]

The curve fitting of the Mn 2p spectra for the LK_dMO ceramics synthesized by the SG, WM, and SS methods is shown in Fig. 10, and the fitting data are summarized in Table 3. The Mn $2p_{3/2}$ peaks for the SG, WM, and SS samples are recorded at binding energies of 641.5 eV, 641.3 eV, and 641.2 eV, respectively, while the Mn $2p_{1/2}$ peaks are recorded at 643.2 eV, 643.1 eV, and 643.0 eV, respectively. The binding energies of Mn 2p should be close to those of Mn_2O_3 and MnO_2.[71,72] Therefore, the LK_dMO ceramics consist of two valence states, Mn^{3+} and Mn^{4+}. This finding is consistent with previous reports.[48,73,74] The Mn 2p peaks for the SG, WM, and SS samples did not show significant changes and were close to the values observed for the studied perovskite materials. The Mn^{3+}/Mn^{4+} ratios for the SG, WM, and SS samples are 2.41, 2.33, and 2.36, respectively. The WM sample shows a ratio value that is close to the theoretical value of 7/3 (2.33). The proportions of Mn^{3+} and Mn^{4+} valence states are influenced by the oxygen concentration, which affects the double-exchange mechanism.[67,75]

According to the literature, manganese oxides exhibit three valence states of oxygen: divalent oxygen ions (O^{2-}), monovalent oxygen ions (O^{-}), and chemically absorbed oxygen (O^{chem}) at binding energies of 529, 530, and 532 eV, respectively.[44] O^{2-} and O^{-} represent lattice oxygen due to Mn–O and La/K–O bonds, respectively, while O^{chem} is likely attributed to oxygen vacancies associated with hydroxyl (OH) and carbon oxide (C–O) states.[76,77] The O 1s ion at the lowest binding energy level (at 529 eV) is associated with the strong covalent Mn–O bond. Additionally, the O 1s spectrum peak at a binding energy of 530 eV is linked to the bond between La/K and O, or a combination of both, because the ionic La/K–O bond requires a higher binding energy compared to the covalent Mn–O bond.[76] The highest binding energy peak, at 532 eV, may result from surface species, such as carbonyl groups or crystal lattice defects. It is said that elements on the outermost surface have higher binding energies. This indicates that surface sites often exhibit lower stability compared to bulk sites.[78] Fig. 11 shows these as O^{2-}, O^{-}, and O^{chem} at binding energies close to 529, 530, and 532 eV, respectively. The ratio of O^{2-} to (O^{2-} + O^{-} + O^{chem}) plays a crucial role in the double-exchange (DE) mechanism. The $O^{2-}/(O^{2-} + O^{-} + O^{chem})$ ratios for the SG, WM, and SS samples were 0.3955, 0.3987, and 0.3983, respectively. The WM sample produces more O^{2-} ions compared to the other samples, indicating an enhancement of the double exchange (DE) mechanism. O^{2-} ions mediate the hopping of electrons between Mn^{3+} and Mn^{4+}. The electron transfer from Mn^{3+} to Mn^{4+} involves the overlap of Mn 3d orbitals with the O 2p orbital, allowing an electron to hop from Mn^{3+} to Mn^{4+} through O^{2-}. This hopping is spin-dependent and highly influenced by the relative alignment of the Mn spins, which directly affects the conductivity of the material. Because manganites are sintered under sufficient oxygen conditions, the concentration of Mn^{4+} can increase, and the substitutional ions can lead to lattice expansion (Table 4).[79]

3.4 Magnetic properties

The magnetic properties were evaluated by measuring the magnetization as a function of the magnetic field (H) for the $La_{0.85}K_{0.1}\square_{0.05}MnO_3$ material at room temperature under 1 T of the applied magnetic fields. The VSM results are shown in Fig. 12. The magnetization curve indicates that all samples show soft magnetic behavior, characterized by low remanent magnetization (M_r) and low coercivity (H_c). The maximum magnetization (M_{max}) values for the SG, WM, and SS samples are 3.544, 6.619, and 6.071 emu g^{-1}, respectively. The magnetization of the SS sample was higher than that of the SG sample. Pan *et al.* reported that an increase in the average grain size leads to an enhancement in the magnetization values.[45] The

Table 3 XPS fitting results of Mn 2p spectra of LK_dMO synthesised using the SG, WM, and SS methods

		Mn $2p_{3/2}$		Mn $2p_{1/2}$		
Preparation method	Valence	Peak position (eV)	Area	Peak position (eV)	Area	$Mn^{3+}/Mn^{4+}(7/3 = 2.33)$
SG	Mn^{3+}	641.57	36 786.05	652.82	19 171.98	2.41
	Mn^{4+}	643.56	13 509.66	654.93	9648.849	
WM	Mn^{3+}	641.45	32 301.92	652.94	16 333.07	2.33
	Mn^{4+}	643.21	16 333.07	654.93	7794.372	
SS	Mn^{3+}	641.22	28 081.18	652.98	22 018.79	2.36
	Mn^{4+}	643.21	15 234.21	654.70	6029.096	

Table 4 XPS fitting results of O 1s spectra of LK_dMO synthesised using the SG, WM, and SS methods

	Peak position (eV)			Area			
Preparation method	O^{2-}	O^{-}	O^{chem}	O^{2-}	O^{-}	O^{chem}	$O^{2-}/(O^{2-} + O^{-} + O^{chem})$
SG	529.26	530.62	531.62	34 327.94	28 651.66	23 811.21	0.3955
WM	529.36	530.91	531.59	33 897.84	29 819.7	21 285.11	0.3987
SS	529.25	530.64	531.37	34 981.99	29 467.12	23 370.2	0.3983

magnetic properties of a material depend on the grain size. When the grain size decreases, it results in an increased number of grain boundaries, which leads to increased magnetic disorder and a weakening of ferromagnetic connectivity.[33] Oumezzine *et al.* also reported that the formation of grain boundaries results in damaged bonds on the surface of the material, which decreases magnetization.[40] The magnetization increased with the application of a higher magnetic field. The magnetic properties and electron transport related to the double-exchange (DE) interaction are controlled by the bandwidth (W), which is determined by the average radii of the cations at the site r_A through the Mn–O–Mn angle ($\theta_{Mn-M-Mn}$) as described by the following equation:

$$W = \frac{\cos\frac{1}{2}(\pi - \langle Mn - O - Mn\rangle)}{d_{\langle Mn-O\rangle}{}^{3.5}}, \quad (3)$$

where $\langle$Mn–O–Mn$\rangle$ is the Mn–O–Mn bond angle and Mn–O–Mn, $d_{\langle Mn-O\rangle}$ is the Mn–O bond length.[80] The results of the bandwidth (W) calculations are summarized in Table 5. Bandwidth (W) decreased with reduced electron mobility in the e_g orbitals owing to a decrease in the Mn–O–Mn bond angle and an increase in the Mn–O bond length, which weakens the double-exchange (DE) interaction.[81] K-site substitution can enhance the ferromagnetic exchange interaction by modifying the bond shape and the Mn^{3+}/Mn^{4+} ratio. This improved interaction reduces resistance and greatly increases MR by improving electron spin alignment when a magnetic field is applied. Certain magnetic phases can also be stabilized by potassium doping, particularly when magnetic fields are applied. By reducing scattering effects and enabling a more transparent conduction channel, especially at lower temperatures, this stability aids MR.[82] The bandwidth (W) calculations show that the WM sample has a higher W value than the SG and SS samples. Therefore, it is reasonable that based on the experimental results, the WM sample exhibits higher magnetization values compared to the SG and SS samples because the increase

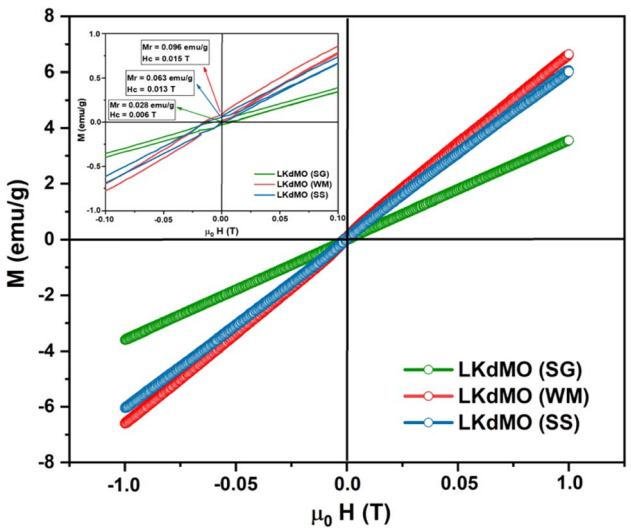

Fig. 12 VSM results of the $La_{0.85}K_{0.1}\square_{0.05}MnO_3$ compound synthesized using the SG, WM, and SS methods.

Table 5 Magnetization (M) and bandwidth (W) values of LK_dMO synthesized through the SG, WM, and SS methods

	LK_dMO		
Parameter	SG	WM	SS
M_{max} (emu g^{-1})	3.544	6.619	6.071
Bandwidth (W) = eV	0.091	0.093	0.092
M_r (emu g^{-1})	0.028	0.096	0.063
H_c (T)	0.006	0.015	0.013

in bandwidth (W) leads to an increase in the DE mechanism. The higher magnetization value in the WM sample was also influenced by the greater number of O^{2-} and Mn^{4+} ions present in the WM sample. O^{2-} ions significantly influence the magnetization of manganite. They are integral to the Mn–O bond network, influencing the exchange interactions between Mn ions. The presence of O^{2-} ions supports the stability of the magnetic order as they mediate the double exchange (DE) mechanism between Mn^{3+} and Mn^{4+} ions, which can enhance ferromagnetic behavior and improve magnetization values. Additionally, a higher concentration of O^{2-} can contribute to a more robust magnetic structure, thereby positively affecting the overall magnetic properties of the material. Increased Mn^{4+} ion content in the WM samples also led to an increase in the DE mechanism.[79,83]

3.5 Magnetoresistance and electrical transport properties

The larger radii of K^+ (1.64 Å) compared to that of La^{3+} (1.36 Å) cause a mismatch in ionic radii, leading to distortion in the MnO_6 octahedron lattice and reducing the geometric configuration of LK_dMO for degeneracy. This phenomenon forms the basis of the Jahn–Teller (JT) effect. Substituting K^+ for La^{3+} results in a mixed valence state of Mn^{3+} and Mn^{4+}, maintaining charge neutrality. According to JT and Hund's rules, electrons in Mn^{3+} are divided into two states: (i) three electrons occupy the t_{2g} orbitals, and (ii) one electron occupies the e_g orbital. In the MnO_6 octahedron, electron delocalization occurs from the e_g orbital of Mn^{3+} to the e_g orbital to the Mn^{4+}. The electrons between the t_{2g} and e_g orbitals of Mn^{3+}/Mn^{4+} exhibit parallel spins because of Hund's coupling effect. The delocalized e_g electrons play a crucial role as a medium for electromagnetic interactions with localized t_{2g} orbitals.[44]

Fig. 13 shows the resistivity *versus* temperature graph in the range of 50–300 K for the LK_dMO samples synthesized by applying the SG, WM, and SS methods, and the parental compound. The curve indicates that the samples with K deficiency had a higher resistivity than the parental compound in the measured temperature range. This is because the presence of vacancies increases the random distribution, leading to an increase in the resistance. Fig. 13 shows that the resistivity values of each sample strongly depend on the synthesis conditions. The resistivity increased from that of the WM sample to that of the SS sample, with the highest resistivity observed in the SG sample. The variation in the resistivity values among the samples was influenced by the electron bandwidth (W) in the conduction process. According to the double exchange (DE) mechanism, electronic transitions are

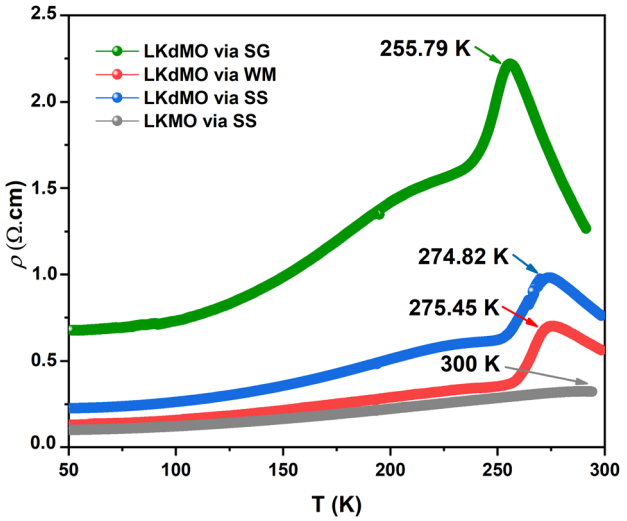

Fig. 13 ρ–T Curves of LK_dMO samples prepared through the SS, WM, and SG methods, and LKMO through SS.

identified by the strong interaction between the Mn^{3+} and Mn^{4+} spins, which enhances conductivity and reduces resistivity.[44] From XPS results, the WM sample produces more O^{2-} ions compared to the other samples. The increase in the number of O^{2-} ions enhances the efficiency of electron transfer and strengthens the spin interactions between manganese ions, thereby improving the conductivity and reducing the resistivity. This explains why the WM sample exhibits better magneto-transport properties than other samples.[83,84]

All samples exhibit transition behavior at the metal–insulator transition temperature (T_ρ) from a metallic phase at low temperatures to an insulating phase at high temperatures. In the region where $T < T_\rho$, the material exhibits a ferromagnetic (FM) phase, which can be explained by double-exchange (DE) interactions. Charge, spin, and magnetic ordering occur at low temperatures. The aligned electron spins at low temperatures cause the angle between Mn^{3+} and Mn^{4+} to align, maximizing electron hopping. Consequently, at low temperatures, LK_dMO exhibited lower resistivity and ferromagnetic properties. Conversely, in the region where $T > T_\rho$, the aligned electron spins are disrupted by strong thermal motion, leading to an increased resistivity and a paramagnetic (PM) phase. From Fig. 13, the T_ρ peaks for the SG, WM, and SS samples were 255.79 K, 274.82 K, and 275.45 K, respectively. LKMO ceramics without K-deficiency showed a T_ρ value of 289 K using the SG and SS methods.[45] This is due to the smaller radius of vacancies compared to La^{3+}, which affects the crystal cell volume. The mismatch in radii at the A-site leads to increased lattice strain, resulting in more distortion. This causes an overlap between the Mn 3d and O 2p orbitals, affecting the decrease in W and shifting T_ρ to lower temperatures. The decrease in T_ρ is also attributed to deviations related to the lower Mn^{4+} content compared to the theoretical value according to the XPS results. This mismatch weakens the DE interaction between Mn^{3+} and Mn^{4+}. The presence of vacancies led to a random distribution, causing the Mn–O–Mn bond angle to deviate from 180°. The mismatch in cationic radii at the A-site, induced by vacancies, lowers the metal–insulator transition temperature in perovskite manganites. Magnetic interactions become more optimal in LK_dMO material due to the combined effects of lattice distortion and increased charge carrier density. Manganites with K-deficient doping exhibit temperature-dependent MR behavior. At certain temperatures, electron hopping reaches an optimal level, where double-exchange interactions and maximum spin alignment occur, resulting in substantial MR.[85]

To determine the effect of the applied magnetic field on the resistivity of the material, the magnetoresistance (MR) was calculated. The MR value is defined by the following equation:

$$\mathrm{MR} = \frac{(\rho_H - \rho_0)}{\rho_0} \times 100\%, \quad (4)$$

where ρ_H is the resistivity of the material under an external magnetic field and ρ_0 is the resistivity without the influence of an external magnetic field.[86] The resistivity *versus* temperature graphs with the application of magnetic fields of 0 T and 2 T for all the samples are shown in Fig. 14. The application of a magnetic field increases the value of T_ρ. This is because the applied magnetic field aligns the electron spin directions and drives a transition from a random to a parallel configuration, thereby reducing resistivity.[87–89] The MR values for the LK_dMO SG, WM, and SS samples are 17.05% at 287.74 K, 54.68% at 271.50 K, and 47.09% at 270.25 K, respectively, showing significant variation. The absolute value of the temperature-dependent MR reaches a maximum near the Curie temperatures (T_C). The K deficiency in the LK_dMO sample led to an increase in MR compared to the MR value of the parental sample (MR = 10.36% at 287 K). This enhancement occurs because the K deficiency disrupts the long-range magnetic order, leading to the formation of short-range ferromagnetic clusters. These clusters increase electrical resistance in the absence of an external magnetic field and exhibit significant changes in the magnetic cluster distribution when an external magnetic field is applied, resulting in an enhanced MR effect. The WM sample shows a substantial decrease in resistivity owing to the smaller grain size, which results in a higher number of grain boundaries acting as scattering centers. Consequently, the magnetic field enhances spin-polarized tunneling, thereby increasing the MR value.[45,90] Additionally, the increase in MR in the WM sample influenced by the Mn^{3+}/Mn^{4+} ratio is closest to the theoretical value.[44] Mn^{4+} ion plays a key role in magnetoresistance (MR), where the resistivity of the material decreases under the influence of an external magnetic field. As Mn^{4+} promotes spin alignment through the double exchange (DE) mechanism, the applied magnetic field can enhance spin order and reduce resistivity, leading to a high MR effect.[79] Furthermore, the SS sample exhibited a higher MR value than the SG sample. This is contradictory, as the SG sample has a smaller grain size than the SS sample and should therefore have more grain boundaries. This may be because of the presence of clustered grains in the micron structure of the SS sample, where some layers of scattering might exist. When subjected to a magnetic field, these layers could enhance the spin-polarized tunneling. Additionally, the reduction in the MR

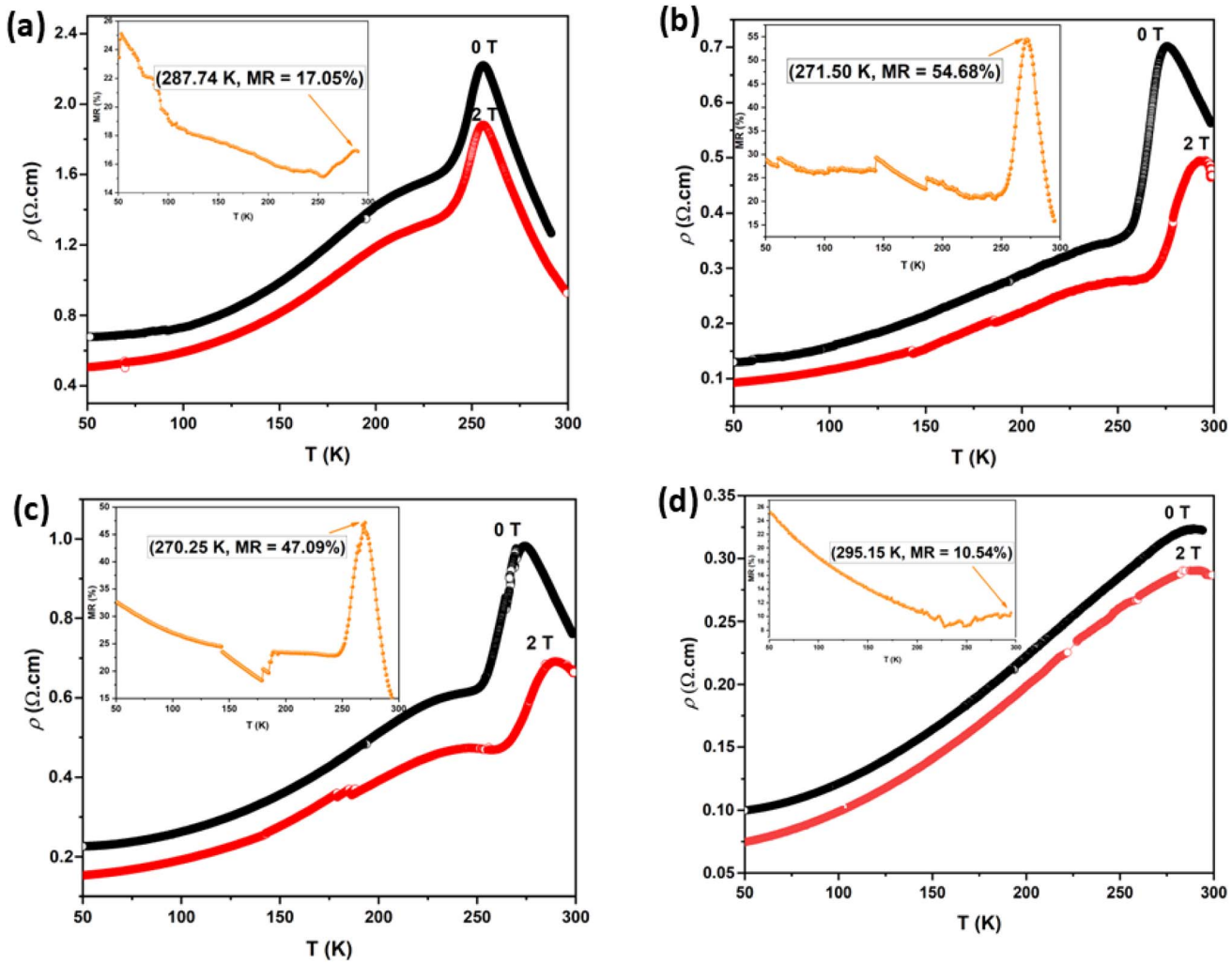

Fig. 14 Resistivity dependence on temperature of LK_dMO ceramics synthesized by employing (a) SG, (b) WM, (c) SS, and (d) the parental compound through SS under 0 and 2 T. Insets show MR dependence temperature plots for LK_dMO and LKMO.

value in the SG sample may be due to the presence of Mn_2O_3 impurities. Owing to the presence of Mn_2O_3 impurities, there was a deficiency of Mn-ions, which consequently resulted in a higher concentration of Mn^{3+} than Mn^{4+}. This results in the super-exchange (SE) interaction between Mn^{3+}–O^{2-}–Mn^{3+} and the formation of an antiferromagnetic (AFI) phase, which causes the MR value and T_ρ to decrease.[52,55]

Fig. 15 shows the field dependence of the magnetoresistance (MR) curve at 150 K for all synthesized LK_dMO samples. The applied magnetic field aligns the electron spins at the grain boundaries. The alignment was enhanced when the external field was increased. Thus, we can observe MR due to a decrease in resistivity for all samples as the applied field increases from 0 kOe to 20 kOe. None of the samples achieved MR saturation with a magnetic field of up to 20 kOe, which means that a higher field is required to align the spins fully. The MR values for all the samples at 150 K did not show significant differences. However, unlike the WM and SS samples, the SG sample did not exhibit an increase in MR within the temperature range of 250–275 K.

The magnetic, electrical, and MR values obtained for the LKMO compounds are summarized in Table 6. Table 6 shows

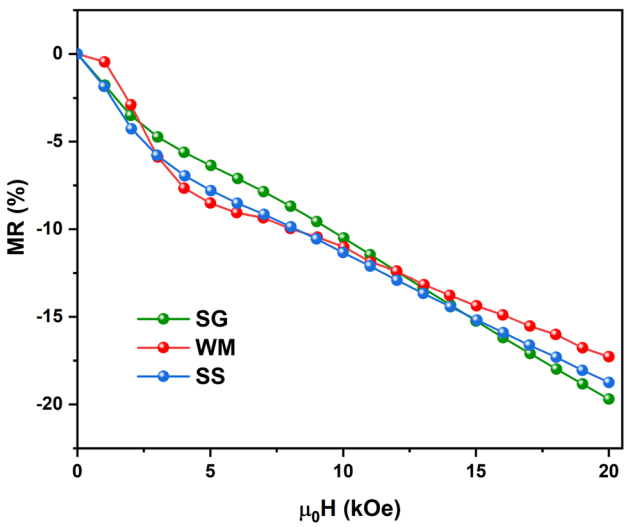

Fig. 15 Field dependence of the MR curve of LK_dMO at 150 K.

Table 6 Magnetoresistance properties with parameters of electrical properties and MR of several LKMO manganites

	Electrical properties		MR				
Sample	$\rho(H)$ (Ω cm)	T_ρ (K)	MR (%)	T_{MR} (K)	$(\mu_0 H)$ B	Method	Ref.
$La_{0.9}K_{0.1}MnO_3$	0.030	300	43.03	286.3	1 T	SG	42
$La_{0.85}K_{0.15}MnO_3$	0.028	>300	46.39	294.03	1 T	SG	42
$La_{0.8}K_{0.2}MnO_3$	0.025	>300	37.49	294.6	1 T	SG	42
$La_{0.75}K_{0.25}MnO_3$	0.020	>300	35.16	295.43	1 T	SG	42
$La_{0.7}K_{0.3}MnO_3$	0.017	>300	26.76	296.4	1 T	SG	42
$La_{0.85}K_{0.1}\square_{0.05}MnO_3$	2.2	255.79	17.05	287.74	2 T	SG	This work
$La_{0.85}K_{0.1}\square_{0.05}MnO_3$	0.7	274.812	54.68	271.50	2 T	WM	This work
$La_{0.85}K_{0.1}\square_{0.05}MnO_3$	1.0	275.45	47.09	270.25	2 T	SS	This work
$La_{0.85}K_{0.15}MnO_3$	0.275	>300	10.36	287	2 T	SS	This work
$La_{0.833}K_{0.167}MnO_3$	2.5	250	0.4	320	5.5 T	SG	91
$La_{0.67}K_{0.33}MnO_3$	22	290	40	300	6 T	SG	4
$La_{0.95}K_{0.05}MnO_3$	0.339	239.8	0.40	300	0.8 T	Thermolysis of an aqueous	15
$La_{0.90}K_{0.10}MnO_3$	0.281	261.9	2.82	300	0.8 T	Thermolysis of an aqueous	15
$La_{0.85}K_{0.15}MnO_3$	0.189	276.0	4.53	300	0.8 T	Thermolysis of an aqueous	15
$LaMnO_{3+\delta}$	5.00	150	0.07	175	0.6 T	Precursor-based synthetic	7
$La_{0.95}$ $K_{0.05}MnO_{3+\delta}$	1.2	230	0.08	225	0.6 T	Precursor-based synthetic	7
$La_{0.85}K_{0.15}MnO_3$	0.1	289	6	300	1 T	SS	45
$La_{0.85}K_{0.15}MnO_3$	1.1	289	3.5	300	1 T	SG	45
$La_{0.85}K_{0.15}MnO_3$	11	258	8	300	1 T	Co-precipitation	45
$La_{0.8}\square_{0.15}MnO_3$	$6.0 \times 10-^5$	300	40	280	2 T	SS	92
La0.8□0.15MnO3	$9.0 \times 10-^5$	290	60	290	5 T	SS	92

that the samples synthesized in this study have parameter values, such as resistivity, T_ρ, and MR, which are similar to those obtained in previous experimental studies. The MR values for the WM and SS samples were relatively high at approximately 270 K. The samples produced under different experimental conditions exhibited significant MR values, demonstrating that different synthesis methods can significantly affect various parameters related to the MR effect. The experimental conditions, including the use of precursors and pH, resulted in varying grain sizes. These differences in grain size play a crucial role in transport processes within the LK_dMO system.

3.6 Conduction mechanism

In the low-temperature FM region ($T < T_\rho$), the temperature-dependent resistivity $\rho(T)$ was approximated using an expression that incorporated several scattering mechanisms, as analyzed based on the following equation:

$$\rho_{FM}(T) = \rho_0 + \rho_2 T^2 + \rho_{4.5} T^{4.5}, \quad (5)$$

where ρ_0 represents the temperature independent resistivity due to grain boundary scattering and plays a crucial role in the conduction process,[93] ρ_2 represents the electrical transport due to electron–electron scattering,[94] and $\rho_{4.5}$ represents the resistivity caused by electron–magnon scattering.[95] In the high-temperature region ($T > T_\rho$), within the PM insulating phase, the electrical resistivity is fitted using the thermally activated behavior, described by the following equation:

$$\rho_{PM}(T) = \rho_\alpha T \exp\left(\frac{E_a}{k_B T}\right), \quad (6)$$

where ρ_α is the residual resistivity, E_a is the activation energy for hopping conduction, and k_B is the Boltzmann constant. In this region, the charge carriers are small polarons, which facilitate conductivity by jumping to the nearest free state.[40]

The electrical transport mechanism across the entire temperature range, particularly around T_ρ, was fitted using a new phenomenological model based on the percolation approach proposed by Li *et al.*[96] The percolation model assumes that the resistivity of the material consists of FM and PM regions. Metallic transport properties are exhibited in the FM regions, whereas insulating properties are displayed in the PM regions. By employing this mechanism, the electrical resistivity across all temperature ranges can be determined using the volume fractions of the FM and PM regions. The resistivity over the entire temperature range can be defined by the following equation:

$$\rho(T) = \rho_{FM} f + \rho_{PM}(1 - f), \quad (7)$$

where f and $1 - f$ represent the volume fractions of the FM and PM regions, respectively. By following the Boltzmann distribution, the functions f and $1 - f$ can be determined through a mathematical combination as follows:

$$f = \frac{1}{1 + \exp\left(\frac{\Delta U}{k_B T}\right)}, \quad (8)$$

$$1 - f = \frac{\exp\left(\frac{\Delta U}{k_B T}\right)}{1 + \exp\left(\frac{\Delta U}{k_B T}\right)}, \quad (9)$$

where ΔU is defined as the energy difference between the FM and PM phases, and it is determined using the following equation:

$$\Delta U = -U_0\left(1 - \frac{T}{T_C^{mod}}\right). \quad (10)$$

Thus, the temperature-dependent resistivity for the entire temperature range can be defined using eqn (11):

$$\rho(T) = \rho_0 + \rho_2 T^2 + \rho_{4.5} T^{4.5} \cdot \frac{1}{1 + e\left(\frac{-U_0\left(1 - \frac{T}{T_C^{mod}}\right)}{k_B T}\right)} + \rho_\alpha T \exp\frac{E_a}{k_B T} \cdot \frac{e\left(\frac{-U_0\left(1 - \frac{T}{T_C^{mod}}\right)}{k_B T}\right)}{1 + e\left(\frac{-U_0\left(1 - \frac{T}{T_C^{mod}}\right)}{k_B T}\right)}. \quad (11)$$

Eqn (11) is in good agreement with our experimental data in the temperature range of 50–300 K. The excellent match between the calculated data (solid red line) and experimental data (black dots) is clearly shown in Fig. 16. The parameters obtained across the entire temperature range, namely ρ_0, ρ_2, $\rho_{4.5}$, ρ_α, E_a/k_B, U_0/k_B, and T_C^{mod}, are summarized in Table 7. The values of ρ_0, ρ_2, and ρ_α for the LK_dMO SG, WM, SS, and parental compound samples showed some differences. The resistivity due to electron–electron scattering (ρ_2) was higher than the resistivity caused by electron–magnon scattering ($\rho_{4.5}$) for all samples (SG, WM, and SS). This indicates that electron–electron scattering is more dominant than electron–magnon scattering in the electron transport process in the FM metallic region ($T < T_\rho$). The results from the percolation fitting indicate that the parameter ρ_0, which represents the resistivity due to grain/domain boundary scattering, increases from the SS to the SG sample. This is reasonable when considering the grain factor, as the SG sample has smaller grains, leading to more grain boundaries than the SS sample. Interestingly, ρ_0 for the WM sample showed the lowest value despite having the smallest grain size. This can be attributed to the higher spin-polarized tunneling at the grain boundaries in the WM sample. Parameter ρ_2, representing

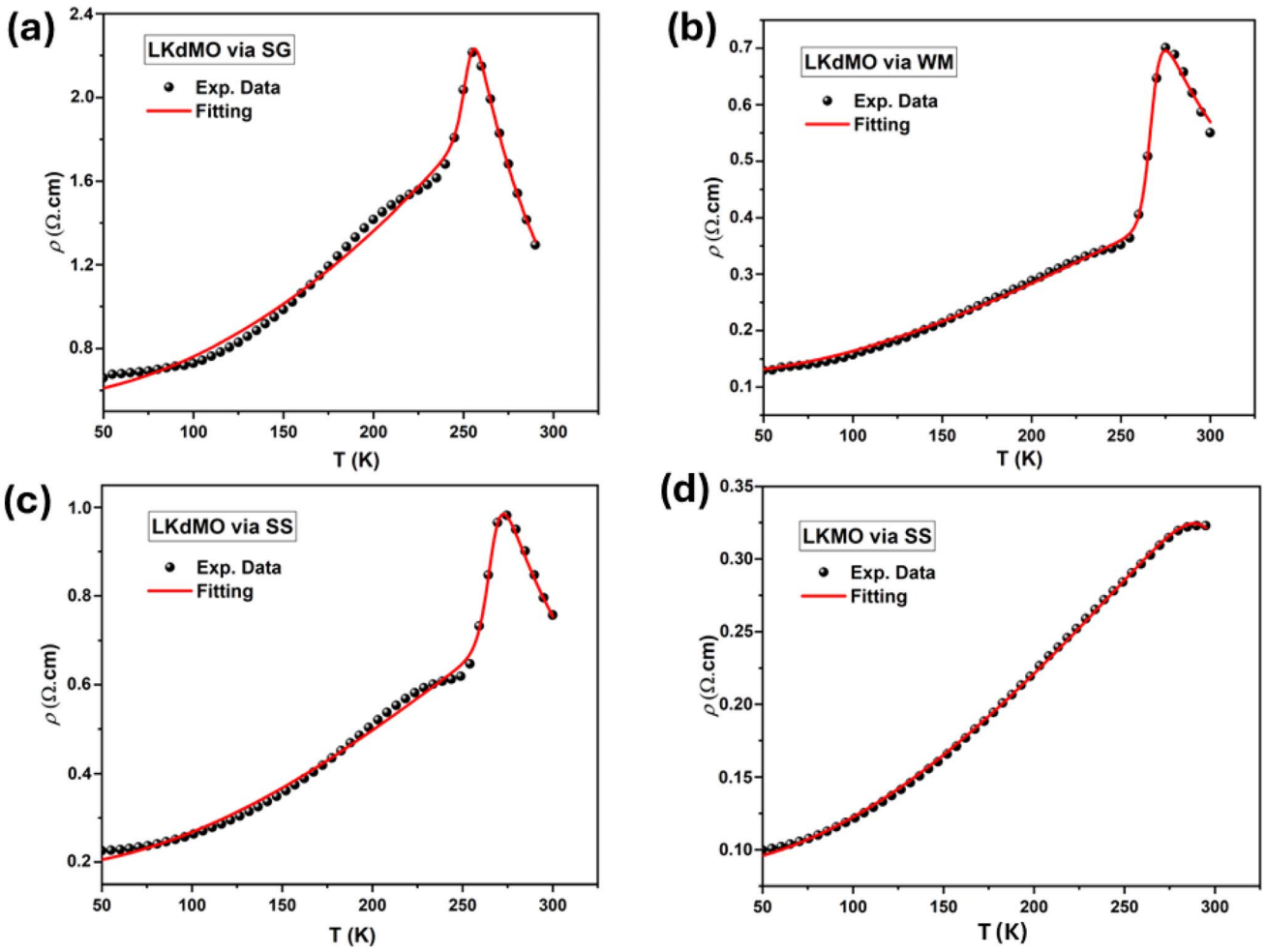

Fig. 16 Fitting curves of ρ–T data in the entire temperature range of the $La_{0.85}K_{0.1}\square_{0.05}MnO_3$ samples by (a) SG, (b) WM, and (c) SS and (d) parental compound. Symbols are the experimental results and solid lines are the fitting using eqn (11).

Table 7 Fitting electrical resistivity parameters of LK_dMO polycrystalline ceramics prepared by employing the SS, WM, and SS methods and LKMO by employing SS

		LK_dMO			LKMO
Region	Parameter	SG	WM	SS	SS
Metallic region	ρ_0 (Ω m)	0.56085	0.12050	0.18452	0.08688
	ρ_2 (Ω m)	2.01511×10^{-5}	4.39968×10^{-6}	8.43211×10^{-6}	3.59854×10^{-6}
	$\rho_{4.5}$ (Ω m)	-2.13622×10^{-13}	-5.82457×10^{-13}	-1.08629×10^{-12}	-4.32522×10^{-13}
Insulator region	ρ_α (Ω m)	2.14489×10^{-5}	5.91243×10^{-5}	4.31794×10^{-5}	8.98083×10^{-6}
	E_a/k_B	1552.26062	1040.83009	1218.95178	1262.01042
Supplement parameter	U_0/k_B	22 933.9676	25 748.72826	21 568.02083	7883.79956
	T_C^{mod}	253.07	267.35	266.56	315.84

electrical transport due to electron–electron scattering, also shows an increase in resistivity across the WM, SS, and SG samples. WM sample has the lowest resistivity. ρ_2 can correlate with the Mn^{4+} concentration from the XPS results, where the WM sample has the highest Mn^{4+} concentration. Mn^{4+} ions play a crucial role in electron transport and the double exchange (DE) mechanism. Additionally, E_a, which represents activation energy for hopping conduction, can be related to the electron bandwidth (W). The SG sample exhibited the highest E_a value among all the samples, corresponding to its lowest W value. A lower W indicates that electrons find it more difficult to move, reducing conductivity and increasing the ability of charge localization. Consequently, electron hopping requires more energy in the SG sample. Furthermore, the value of T_C^{mod} shows a slight variation from T_ρ, influenced by the existence of magnetic bi-phase states, including ferromagnetic and antiferromagnetic states, owing to strong s–d exchange.[97]

4. Conclusions

LK_dMO ceramics were successfully synthesized using SG, WM, and SS methods, and the results were compared. The structure, magnetic properties, and electrical transport properties were studied using XRD, SEM, EDS, XPS, VSM, and FPP. No differences in the crystal phases and elements of the perovskite manganite materials were observed among the SG, WM, and SS samples. LK_dMO ceramics produced using WM and SS exhibited a single phase belonging to the $R\bar{3}c$ space group with a rhombohedral structure, while the SG sample showed the presence of a secondary Mn_2O_3 phase. The EDS and XPS results suggested that La, K, Mn, and O were uniformly distributed in the samples. The SEM results indicated that the WM sample had a smaller average grain size than the SG and SS samples. Consequently, the WM sample exhibited lower resistivity owing to the reduced scattering of the grain boundaries. However, the difference in grain size owing to the synthesis method affects the transport and magnetic performance. The highest MR values for the SG, WM, and SS samples were 17.05% at 287.74 K, 54.68% at 271.50 K, and 47.09% at 270.25 K, respectively. The K-site deficiency successfully enhanced the MR value in the LK_dMO material compared to the parental compound (LKMO), achieving an MR value of 10.36% at 287 K. Compared with the SG and SS samples, the WM sample exhibited the highest MR, which was attributed to the enhancement of spin-polarized tunneling by the largest grain boundary contribution. Overall, the WM method is more effective for producing LK_dMO polycrystalline ceramics with better crystal quality and electromagnetic properties. Our results show that K-deficient formation can improve MR by changing the manganite lattice, which probably changes the structure and makes it easier for electrons to move around. These findings contribute to resolving inconsistencies in this field and highlight the potential for simpler, scalable synthesis methods for practical applications. Future work will focus on optimizing synthesis conditions to precisely control defect densities and types, with the aim of achieving an optimal balance that maximizes MR.

Data availability

The data supporting our research are solely generated by us. The data that support the findings of this study are available from the corresponding author, upon reasonable request.

Conflicts of interest

The authors declare no conflict of interest.

Acknowledgements

The authors gratefully acknowledge the PMDSU Scholarship awarded to Okvarahireka Vitayaya and the financial support under grant "Hibah Publikasi Terindeks Internasional (PUTI) Q2 2024-2025" NKB-677/UN2.RST/HKP.05.00/2024.

References

1 A. Ezaami, I. Sfifir, W. Cheikhrouhou-Koubaa, M. Koubaa and A. Cheikhrouhou, *J. Alloys Compd.*, 2017, **693**, 658–666.
2 J. M. D. Coey, M. Viret and S. Von Molnár, *Adv. Phys.*, 1999, **48**, 167–293.
3 S. Atalay, V. S. Kolat, H. Gencer and H. I. Adiguzel, *J. Magn. Magn. Mater.*, 2006, **305**, 452–456.
4 A. Goktas, I. H. Mutlu and A. Kawashi, *Thin Solid Films*, 2012, **520**, 6138–6144.

5 A. Urushibara, Y. Moritomo, T. Arima, A. Asamitsu, G. Kido and Y. Tokura, *Phys. Rev. B:Condens. Matter Mater. Phys.*, 1995, **51**, 14103–14109.
6 T. Sun, F. Ji, Y. Liu, G. Dong, S. Zhang, Q. Chen and X. Liu, *J. Eur. Ceram. Soc.*, 2019, **39**, 352–357.
7 Y. Ng-Lee, F. Sapiña, E. Martinez-Tamayo, J. V. Folgado, R. Ibañez, D. Beltrán, F. Lloret and A. Segura, *J. Mater. Chem.*, 1997, **7**, 1905–1909.
8 Y. Kalyana Lakshmi, G. Venkataiah, M. Vithal and P. Venugopal Reddy, *Phys. B*, 2008, **403**, 3059–3066.
9 N. Phahul Zhemas Zul, O. Vitayaya, D. Rezky Munazat, M. T. E. Manawan and D. Darminto, *Phys. Chem. Chem. Phys.*, 2024, **26**, 14476–14504.
10 S. Joseph and K. V. Saban, *Ceram. Int.*, 2019, **45**, 6425–6439.
11 A. P. Ramirez, *J. Phys.:Condens. Matter*, 1997, **9**, 8171–8199.
12 C. Zener, *Phys. Rev.*, 1951, **82**, 403–405.
13 M. Sahana, M. S. Hegde, C. Shivakumara, V. Prasad and S. V. Subramanyam, *J. Solid State Chem.*, 1999, **148**, 342–346.
14 B. Kurniawan, S. Winarsih, A. Imaduddin and A. Manaf, *Phys. B*, 2018, **532**, 161–165.
15 S. Das and T. K. Dey, *Solid State Commun.*, 2005, **134**, 837–842.
16 G. Huo, Z. Gu, S. Liu, Y. Wang and Y. Wang, *J. Alloys Compd.*, 2007, **433**, 41–45.
17 A. G. Gamzatov, A. B. Batdalov, O. V. Melnikov and O. Y. Gorbenko, *Low Temp. Phys.*, 2009, **35**, 219–222.
18 W. Boujelben, A. Cheikh-Rouhou and J. C. Joubert, *Eur. Phys. J. B*, 2001, **24**, 419–423.
19 M. Ellouze, W. Boujelben, A. Cheikhrouhou, H. Fuess and R. Madar, *Solid State Commun.*, 2002, **124**, 125–130.
20 W. Cheikh-Rouhou Koubaa, M. Koubaa, A. Cheikh-Rouhou, W. Boujelben and A. M. Haghiri-Gosnet, *J. Alloys Compd.*, 2008, **455**, 67–72.
21 S. K. Mandal, T. K. Nath and V. V. Rao, *J. Phys.:Condens. Matter*, 2008, **20**, 385203.
22 T. Sarkar, B. Ghosh, A. K. Raychaudhuri and T. Chatterji, *Phys. Rev. B:Condens. Matter Mater. Phys.*, 2008, **77**, 1–9.
23 S. V. Trukhanov, L. S. Lobanovski, M. V. Bushinsky, I. O. Troyanchuk and H. Szymczak, *J. Phys.:Condens. Matter*, 2003, **15**, 1783–1795.
24 A. De Andrés, M. García-Hernández and J. L. Martínez, *Phys. Rev. B:Condens. Matter Mater. Phys.*, 1999, **60**, 7328–7334.
25 H. Y. Hwang, S. W. Cheong, P. G. Radaelli, M. Marezio and B. Batlogg, *Phys. Rev. Lett.*, 1995, **75**, 914–917.
26 P. Lyu, D. Xing and J. Dong, *Phys. Rev. B:Condens. Matter Mater. Phys.*, 1998, **58**, 54–57.
27 M. Viret, M. Drouet, J. Nassar, J. P. Contour, C. Fermon and A. Fert, *Europhys. Lett.*, 1997, **39**, 545–549.
28 L. Balcells, J. Fontcuberta, B. Martínez and X. Obradors, *Phys. Rev. B:Condens. Matter Mater. Phys.*, 1998, **58**, R14697–R14700.
29 R. Shreekala, M. Rajeswari, K. Ghosh, A. Goyal, J. Y. Gu, C. Kwon, Z. Trajanovic, T. Boettcher, R. L. Greene, R. Ramesh and T. Venkatesan, *Appl. Phys. Lett.*, 1997, **71**, 282–284.
30 J. M. D. Coey, M. Viret and L. Ranno, *Phys. Rev. Lett.*, 1995, **75**, 3910–3913.
31 R. M'Nassri, N. Chniba Boudjada and A. Cheikhrouhou, *J. Alloys Compd.*, 2015, **626**, 20–28.
32 S. Mahjoub, M. Baazaoui, E. K. Hlil and M. Oumezzine, *Ceram. Int.*, 2015, **41**, 12407–12416.
33 M. R. Laouyenne, M. Baazaoui, K. Farah, E. K. Hlil and M. Oumezzine, *J. Magn. Magn. Mater.*, 2019, **474**, 393–399.
34 D. R. Munazat, B. Kurniawan, D. S. Razaq, K. Watanabe and H. Tanaka, *Phys. B*, 2020, **592**, 412227.
35 B. Vertruyen, A. Rulmont, R. Cloots, M. Ausloos, S. Dorbolo and P. Vanderbemden, *Mater. Lett.*, 2002, **57**, 598–603.
36 A. K. M. Akther Hossain, L. F. Cohen, F. Damay, A. Berenov, J. MacManus-Driscoll, N. M. Alford, N. D. Mathur, M. G. Blamire and J. E. Evetts, *J. Magn. Magn. Mater.*, 1999, **192**, 263–270.
37 C. Vázquez-Vázquez, M. Carmen Blanco, M. Arturo López-Quintela and R. D. Sánchez, *J. Mater. Chem.*, 1998, **1998**(8), 991–1000.
38 A. Selmi, W. Cheikhrouhou-Koubaa, M. Koubaa and A. Cheikhrouhou, *J. Supercond. Novel Magn.*, 2013, **26**, 1421–1428.
39 R. M'nassri, W. Cheikhrouhou-Koubaa, M. Koubaa and A. Cheikhrouhou, *IOP Conf. Ser.:Mater. Sci. Eng.*, 2012, **28**, 0–8.
40 M. Oumezzine, S. Hcini, M. Baazaoui, H. B. Sales, I. M. G. Dos Santos and M. Oumezzine, *J. Alloys Compd.*, 2013, **571**, 79–84.
41 L. N. Lau, K. P. Lim, A. N. Ishak, M. M. Awang Kechik, S. K. Chen, N. B. Ibrahim, M. Miryala, M. Murakami and A. H. Shaari, *Coatings*, 2021, **11**, 361.
42 S. Jin, X. Gu, X. Yu, X. Guan, Y. Yan, K. Wu, L. Zhao, Y. Zhu, S. Sun, J. Liu, J. Hu, J. Zhao, L. Kong, W. Yang, Q. Chen, P. Kameli and X. Liu, *Appl. Surf. Sci.*, 2022, **589**, 152905.
43 R. Dhahri and F. Halouni, *J. Alloys Compd.*, 2004, **381**, 21–25.
44 X. Yu, H. Li, K. Chu, X. Pu, X. Gu, S. Jin, X. Guan and X. Liu, *Ceram. Int.*, 2021, **47**, 13469–13479.
45 K. Y. Pan, S. A. Halim, K. P. Lim, W. M. W. Y. Daud, S. K. Chen and M. Navasery, *J. Mater. Sci.:Mater. Electron.*, 2013, **24**, 1869–1874.
46 B. Rajyaguru, K. Gadani, M. J. Keshvani, D. Dhruv, A. D. Joshi, K. Asokan, R. J. Choudhary, D. M. Phase, N. A. Shah and P. S. Solanki, *Mater. Res. Bull.*, 2024, **170**, 112548.
47 F. Elleuch, M. Triki, M. Bekri, E. Dhahri and E. K. Hlil, *J. Alloys Compd.*, 2015, **620**, 249–255.
48 B. Arun, V. R. Akshay and M. Vasundhara, *Dalton Trans.*, 2018, **47**, 15512–15522.
49 S. Jin, S. Zhang, X. Yu, X. Guan, H. Li, K. Chu, X. Pu, X. Gu and X. Liu, *Ceram. Int.*, 2021, **47**, 24721–24731.
50 N. A. Liedienov, A. V. Pashchenko, V. P. Pashchenko, V. K. Prokopenko, D. D. Tatarchuk, Y. F. Revenko, V. A. Turchenko, V. V. Burchovetskii, V. Y. Sycheva, A. G. Sil'cheva, Y. V. Didenko and G. G. Levchenko, *Low Temp. Phys.*, 2017, **43**, 1076–1085.
51 C. Henchiri, R. Hamdi, T. Mnasri, M. A. Valente, P. R. Prezas and E. Dhahri, *Appl. Phys. A:Mater. Sci. Process.*, 2019, **125**, 1–19.

52 A. Zahrin, N. A. Azhar, N. Ibrahim and Z. Mohamed, *Condens. Matter*, 2022, **7**, 51.
53 C. Luo, Y. Zheng, Y. Xu, N. Ding, Q. Shen and C. Zheng, *Chem. Eng. J.*, 2015, **267**, 111–116.
54 N. Soylu Koc, S. P. Altintas, N. Mahamdioua and C. Terzioglu, *J. Alloys Compd.*, 2019, **797**, 471–476.
55 M. A. I. Zainuddin, R. Rozilah, N. Ibrahim and Z. Mohamed, *J. Alloys Compd.*, 2024, **976**, 173225.
56 R. V. Lakshmi, P. Bera, M. Hiremath, V. Dubey, A. K. Kundu and H. C. Barshilia, *Phys. Chem. Chem. Phys.*, 2022, **24**, 5462–5478.
57 S. S. Teixeira, F. Amaral, M. P. F. Graça and L. C. Costa, *Mater. Sci. Eng., B*, 2020, **255**, 114529.
58 M. Khlifi, E. Dhahri and E. K. Hlil, *J. Alloys Compd.*, 2014, **587**, 771–777.
59 R. Atanasov, R. Bortnic, R. Hirian, E. Covaci, T. Frentiu, F. Popa and I. G. Deac, *Materials*, 2022, **15**, 7645.
60 R. Tlili, M. Bejar, E. Dhahri, A. Zaoui, E. K. Hlil and L. Bessais, *Polyhedron*, 2017, **121**, 19–24.
61 Z. Wei, N. A. Liedienov, Q. Li, A. V. Pashchenko, W. Xu, V. A. Turchenko, M. Yuan, I. V. Fesych and G. G. Levchenko, *Ceram. Int.*, 2021, **47**, 24553–24563.
62 M. W. Shaikh and D. Varshney, *Mater. Chem. Phys.*, 2012, **134**, 886–898.
63 G. Kimmel, A. Sahartov, Y. Sadia, Z. Porat, J. Zabicky and E. Dvir, *J. Mater. Res. Technol.*, 2021, **12**, 87–99.
64 W. Qin, T. Nagase, Y. Umakoshi and J. A. Szpunar, *Philos. Mag. Lett.*, 2008, **88**, 169–179.
65 Y. Zhang, Y. Zhang, B. Fu, M. Hong, M. Xiang, Z. Liu, H. Liu and S. Liu, *J. Mater. Sci.:Mater. Electron.*, 2015, **26**, 3179–3185.
66 A. White, A. Walpole, Y. Huang and D. L. Trimm, *Appl. Catal.*, 1989, **56**, 187–196.
67 D. R. Munazat, B. Kurniawan, N. Kurita, X. Wang, M. Manawan, T. Sudiro and H. Nojiri, *Phys. Chem. Chem. Phys.*, 2024, **26**, 18343–18367.
68 R. Tripathi, A. Dogra, A. K. Srivastava, V. P. S. Awana, R. K. Kotnala, G. L. Bhalla and H. Kishan, *J. Phys. D Appl. Phys.*, 2009, **42**, 1–6.
69 A. Gupta and G. Gong, *Phys. Rev. B:Condens. Matter Mater. Phys.*, 1996, **54**, R15629–R15632.
70 X. Wang, Y. Chen, W. Quan, T. Masuzawa, Y. Okigawa, S. Ogawa and Y. Takakuwa, *Nano Express*, 2021, **2**, 030004.
71 J. J. Qian, W. H. Qi, Z. Z. Li, L. Ma, G. D. Tang, Y. N. Du, M. Y. Chen, G. H. Wu and F. X. Hu, *RSC Adv.*, 2018, **8**, 4417–4425.
72 P. K. Siwach, P. Srivastava, H. K. Singh, A. Asthana, Y. Matsui, T. Shripathi and O. N. Srivastava, *J. Magn. Magn. Mater.*, 2009, **321**, 1814–1820.
73 B. Arun, V. R. Akshay and M. Vasundhara, *RSC Adv.*, 2019, **9**, 23598–23606.
74 J. Van Elp, R. H. Potze, H. Eskes, R. Berger and G. A. Sawatzky, *Phys. Rev. B:Condens. Matter Mater. Phys.*, 1991, **44**, 1530–1537.
75 Y. Moualhi, M. Smari and H. Rahmouni, *RSC Adv.*, 2023, **13**, 30010–30021.
76 P. R. Nadig, S. Murari and M. D. Daivajna, *Phys. Chem. Chem. Phys.*, 2024, **26**, 5237–5252.
77 D. Kumar and A. K. Singh, *J. Phys. Chem. Solids*, 2023, **176**, 111253.
78 G. Kozhina, V. Mitrofanov, O. Fedorova, A. Fetisov, A. Murzakaev and S. Estemirova, *J. Alloys Compd.*, 2021, **864**, 158816.
79 G. Dong, Y. Liu, S. Zhang, K. Chu, H. Li, X. Pu, T. Sun, F. Ji and X. Liu, *Ceram. Int.*, 2019, **45**, 21448–21456.
80 S. Othmani, M. Bejar, E. Dhahri and E. K. Hlil, *J. Alloys Compd.*, 2009, **475**, 46–50.
81 R. Rozilah, N. Ibrahim and A. K. Yahya, *Solid State Sci.*, 2019, **87**, 64–80.
82 Y. Kalyana Lakshmi, S. Manjunathrao and P. Venugopal Reddy, *Mater. Chem. Phys.*, 2014, **143**, 983–990.
83 R. Dhahri and F. Halouni, *J. Alloys Compd.*, 2004, **385**, 48–52.
84 S. V. Trukhanov, I. O. Troyanchuk, N. V. Pushkarev and H. Szymczak, *J. Exp. Theor. Phys.*, 2002, **95**, 308–315.
85 N. Zurauskiene, V. Stankevic, S. Kersulis, M. Vagner, J. Pietosa and A. Wisniewski, *sensors*, 2022, **22**, 4004.
86 L. Yin, C. Wang and Q. Shen, *Ceram. Int.*, 2023, 1–9.
87 O. Vitayaya, P. Z. Zul Nehan, D. R. Munazat, M. T. E. Manawan and B. Kurniawan, *RSC Adv.*, 2024, **14**, 18617–18645.
88 R. Tripathi, V. P. S. Awana, H. Kishan, S. Balamurugan and G. L. Bhalla, *J. Supercond. Novel Magn.*, 2008, **21**, 151–159.
89 Y. Zhou, X. Zhu and S. Li, *Ceram. Int.*, 2017, **43**, 10026–10031.
90 U. Chand, K. Yadav, A. Gaur and G. D. Varma, *J. Rare Earths*, 2010, **28**, 760–764.
91 W. Jian, *J. Magn. Magn. Mater.*, 2012, **324**, 2183–2187.
92 M. Wali, R. Skini, M. Khlifi, M. Bekri, E. Dhahri and E. K. Hlil, *Ceram. Int.*, 2016, **42**, 5699–5706.
93 A. Dhahri, M. Jemmali, E. Dhahri and E. K. Hlil, *Dalton Trans.*, 2015, **44**, 5620–5627.
94 P. Schiffer, A. P. Ramirez, W. Bao and S. W. Cheong, *Phys. Rev. Lett.*, 1995, **75**, 3336–3339.
95 G. Venkataiah and P. V. Reddy, *Solid State Commun.*, 2005, **136**, 114–119.
96 G. Li, H. D. Zhou, S. J. Feng, X. J. Fan, X. G. Li and Z. D. Wang, *J. Appl. Phys.*, 2002, **92**, 1406–1410.
97 A. G. Gamzatov and I. K. Kamilov, *J. Alloys Compd.*, 2012, **513**, 334–338.